Order Number 1360098

Generation of broad bandwidth UV pulses via sum frequency mixing

Reiten, Matthew Thomas, M.S.

Rice University, 1994

U·M·I
300 N. Zeeb Rd.
Ann Arbor, MI 48106

RICE UNIVERSITY

Generation of Broad Bandwidth UV Pulses via Sum Frequency Mixing

by

Matthew T. Reiten

A THESIS SUBMITTED
IN PARTIAL FULFILLMENT OF THE
REQUIREMENTS FOR THE DEGREE

Master of Science

APPROVED, THESIS COMMITTEE:

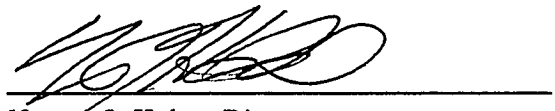

Naomi J. Halas, Director
Assistant Professor of Electrical Engineering

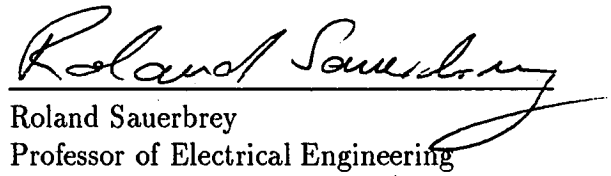

Roland Sauerbrey
Professor of Electrical Engineering

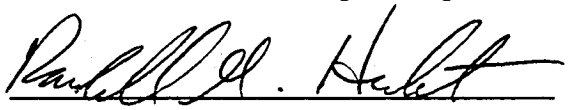

R. Hulet
Associate Professor of Physics

Houston, Texas

April, 1994

Generation of Broad Bandwidth UV Pulses via Sum Frequency Mixing

Matthew T. Reiten

Abstract

Focusing effects on phase front curvature are important in determining the bandwidth generated in the near vacuum ultraviolet by sum frequency mixing of ultrashort pulses. Noncollinear sum frequency mixing is utilized to produce 6.0 eV fourth harmonic radiation of a passively mode-locked titanium doped sapphire laser operating at a high repetition rate. The spectrum of the generated fourth harmonic radiation is broader than would be predicted if focusing is not taken into account. A method of calculating the bandwidth for sum frequency mixing of short pulses is developed and is experimentally supported.

Acknowledgments

I am compelled to thank Dr. Naomi Halas for her professional support and contributions to the course of this research, throughout the various iterations. Dr. Alan Cheville and Rick Averitt, comrades-in-arms, provided friendship and perspective, earning my eternal gratitude. I want to acknowledge my father for his help, most notably the ressurection of the Duster, proving beyond doubt the extent of his love.

Finally, I must thank Beth Moran, whose companionship and love through the darker times of the research process kept me aware of what truly matters in life.

A thousand year journey cannot be made overnight,

unless one starts at noon.

Contents

Illustrations

Tables

Chapter 1

Introduction

Recent interest in the generation of subpicosecond pulses in the near VUV region has been prompted by the introduction of the modelocked titanium doped sapphire laser and the availability of nonlinear optical crystals transparent in the short wavelength region. A variety of applications require ultrashort UV pulses such as producing the seed pulses at 193 nm for an argon fluoride amplifier [1], transient absorption studies of chemical species [2], or time resolved photoemission spectroscopy [3].

Previously, laser pulses in this photon energy range, $\sim$ 6 eV, were commonly generated by mixing the fourth harmonic of a Nd:YAG laser at 266 nm and the 700 nm output of a dye laser pumped by the second harmonic of the same Nd:YAG laser source [4]. In addition to producing long pulses (on the order of nanoseconds), the repetition rate of the pulse train was limited to that of the source, typically below 100 Hz. This and other shortcomings have led researchers to turn to another system for generating short UV pulses.

Problems arise when the pulses become extremely short, the subpicosecond regime. Physical limitations on the materials tend to indicate that the generated pulse will have a minimum duration much larger than the incident pulses. Several schemes have been implemented to overcome this problem [5, 6]. However, the conditions that require efforts to enhance the mixing process are not clear.

A fully solid-state system for generating the fourth harmonic at 205 nm of a passively mode-locked titanium doped sapphire laser is presented here. Chapter 2 covers background material relevant to the discussion of challenges inherent to ultrashort pulse sum frequency mixing. Chapter 3 contains a description of the sum frequency chain and the procedures used to realize the generation of 205 nm light. Two separate cases are examined and the corresponding measurements are given. Chapter 4 presents a method to calculate the resultant bandwidth corresponding to a short pulse from a sum frequency mixing process given the characteristics of the input light and the geometrical configuration. The modeling is then compared to the measured bandwidths and is experimentally verified. Chapter 5 proposes further experimental improvements and presents a conclusion.

Chapter 2

Background

2.1 Sum Frequency Mixing

2.1.1 Nonlinear Polarization

Sum frequency mixing (SFM) is the process where two beams of light interact with a material to produce light at the sum of their frequencies. Associated with this is the process of difference frequency mixing. While frequency up and down conversion may be accomplished in other nonlinear optical (NLO) materials, this discussion will only consider SFM of two beams in a uniaxial crystal, β-barium borate (BBO). There are several treatments of SFM of varying degrees of rigor and involvement. For a clear handling of SFM in applications see [7]. For more detailed texts refer to [8], [9], or [10]. For an interesting review article over the various different types of nonlinear processes, including SFM, see [11].

The interaction of laser light with a crystalline material is described by the induced polarization of the crystal, $\vec{P}$. The applied optical electric field, $\vec{E}$, induces a charge separation in the individual atoms or molecules forming the crystal. $\vec{P}$ will be

proportional to the incident electric field. The constant of proportionality for a bulk material is called the susceptibility, χ, and is a function of frequency.

This charge separation leads to a dipole that reradiates at the same frequency as the incident light. However, if this system is overdriven by an intense electric field, the restoring force on the bound electrons will no longer behave linearly. Considering two incident electric fields, the resulting nonlinear polarization can be described by a Taylor series expansion in the mixing electric fields:

$$\vec{P} = \underbrace{\chi(\vec{E}_1 + \vec{E}_2)}_{\vec{P}_{linear}} + \underbrace{\chi^{(2)}\vec{E}_1\vec{E}_2 + \cdots}_{\vec{P}_{nonlinear}} \tag{2.1}$$

Here, χ is the linear susceptibility and $\chi^{(2)}$ is a third rank tensor for determining the second-order nonlinear susceptibility. As SFM is a second-order effect, all higher order processes will be neglected in this treatment. The contributions from the $\chi^{(2)}$ tensor are generally small, so in order to produce observable SFM, the strength of the incident electric field must be high. This has been accomplished through the use of laser radiation.

The dipoles induced by the incident electric fields reradiate as determined by the polarization. The linear response will be ignored as the nonlinear effects are of interest here. Assuming that the two incident electric fields oscillate at different frequencies,

ω_1 and ω_2, the nonlinear polarization can be expressed as

$$\vec{P}_{nonlinear} = \sum_{i,j,k,n,m} \hat{a}_i \chi^{(2)}_{ijk} E_j(\omega_n) E_k(\omega_m) e^{-i(\omega_n+\omega_m)t}. \tag{2.2}$$

The $\chi^{(2)}$ tensor is nonzero only in materials that lack inversion symmetry. Due to the permutations of the two electric field components, it is possible to generate radiation at $\omega_1 + \omega_2$ and $|\omega_1 - \omega_2|$. These two cases are sum frequency mixing and difference frequency mixing, respectively. Second harmonic generation (SHG) is a special case of SFM where $\vec{E}_1$ is at the same frequency as $\vec{E}_2$.

From this point, all conceptual development will focus on SFM. The same treatment holds for difference frequency mixing.

2.1.2 Phase Matching

The reradiation of light from the induced dipoles undergoes a phase shift with respect to the incident field. This results in a retardation of the phase velocity of light being transmitted through the material. This reduced phase velocity in a material is described by the index of refraction, $n(\omega, \theta)$, a function of the frequency of light, ω, and, in general, the direction of propagation through the material, θ.

In SFM, two input beams of different frequencies interact in the nonlinear crystal and produce a second-order induced polarization. Though the phase velocity is

different for each beam, the phase of the induced polarization will be constant. If the summed frequency experiences a different index of refraction, the nonlinear polarization and the generated light will soon move out of phase. The newly generated summed frequency can interfere destructively with the previously generated light, reducing the output power. To overcome this problem, the phase velocities of the induced polarization and the generated sum frequency light must be equal for efficient conversion of energy.

Conservation of energy requires that $\hbar(\omega_1 + \omega_2) = \hbar\omega_3$. Phase matching is an expression of conservation of momentum. In a vectorial representation, SFM phase matching requires $\vec{k}_1 + \vec{k}_2 = \vec{k}_3$ where $\vec{k}_n$ is the wavevector of the light at the appropriate frequency. The phase mismatch is defined as

$$\Delta k = |\vec{k}_1 + \vec{k}_2 - \vec{k}_3|. \tag{2.3}$$

When $\Delta k = 0$, the SFM process is said to be phase matched. The magnitude of the wave vectors are related to the index of refraction of the material by the following relation,

$$k = \frac{n(\omega, \theta)\omega}{c}. \tag{2.4}$$

The frequencies involved have been fixed by the energy requirement. The index of refraction in Equation 2.4 is the only variable that can be modified in order to satisfy the momentum requirement of Equation 2.3. Many birefringent crystals allow phase matching to occur for SFM. The index of refraction may be varied in birefringent materials, such as BBO, through the method of angle tuning.

The index of refraction experienced by a beam of light in a birefringent NLO crystal is dependent upon the polarization of the optical field and the direction of propagation. Through proper alignment, these angular relationships in birefringent crystals may be exploited such that the input light can experience the proper index of refraction to phase match with the generated sum frequency.

The intensity of the output sum frequency light is proportional to the product of the mixing intensities modified by a functional dependence upon the phase mismatch. Assuming no power is depleted from the input beams, the intensity for mixing plane waves is given by

$$I_{SFM} = \left[\frac{512 \times 10^{-7}\pi^5 d_{eff}^2 I_1 I_2 L^2}{c n_1 n_2 n_{SFM} \lambda_{SFM}^2}\right] \frac{\sin^2\left(\frac{\Delta k \cdot L}{2}\right)}{\left(\frac{\Delta k \cdot L}{2}\right)^2}. \tag{2.5}$$

I_{SFM}, I_1, and I_2 are the square of the appropriate electric field per unit area expressed in W/cm^2. L is the length of the crystal given in the same units as λ_{SFM}, the

wavelength of the sum frequency in vacuum. d_{eff} is the effective nonlinear coefficient which is derived from the $\chi^{(2)}$ tensor [7] and is given in c.g.s. units. n_1, n_2, and n_{SFM} are the indices of refraction for the appropriate beam. Δk is the phase mismatch as defined in Equation 2.3. The factor of $512 \times 10^{-7}\pi^5/c$ arises from the hybrid units and starting from unrationalized Maxwell's equations.

2.2 Ultrashort Pulses

2.2.1 Theory

Since the intensity of the generated fourth harmonic light is determined by the product of the square of the electric fields of both input beams, it is clear that in order to achieve a high conversion efficiency, large peak powers must be used. Short pulse lasers can deliver high peak intensities. While some lasers are capable of producing Terawatt range peak intensities, even a modest laser system producing a few hundred milliwatts of continuous power when emitting subpicosecond pulses can generate peak intensities greater than hundreds of Megawatts/cm^2 when focused.

Certain aspects of the behavior of light come into play when the pulses are reduced to subpicosecond durations [12, 13]. A short pulse, taken to be propagating in the z direction as an example, can be expressed in time as a plane wave modified by an

envelope function:

$$\vec{E} = E(t) \exp^{-i(\omega t - kz)} \hat{a}_z. \tag{2.6}$$

As a direct consequence of the Fourier transformation relationships between time and frequency, there is a fixed relation between the temporal pulse width and the spectral bandwidth of a given ultrashort pulse. A short pulse in time will have a wide spectral distribution. This is usually described by

$$\Delta t \Delta \omega \geq const., \tag{2.7}$$

or, in terms of wavelength and time,

$$\frac{c}{\lambda^2} \Delta t \Delta \lambda \geq const. \tag{2.8}$$

Equations 2.7 and 2.8 are referred to as the time-bandwidth product. Δt is the temporal pulse width. $\Delta\omega$ and $\Delta\lambda$ are the width of the spectrum in frequency and wavelength respectively. For this treatment, the width of the pulse and spectrum will be taken as the standard full width at half maximum (FWHM). c is the speed of light. The constant is dependent upon the shape of the envelope and the definition of the measurements [14].

2.2.2 Measurement

Cross Correlation

Electronics do not have a subpicosecond response time and therefore cannot resolve the pulsewidths of subpicosecond optical pulses. The direct temporal measurement of subpicosecond laser pulses is accomplished through cross correlation techniques.

The experimental geometry for cross correlation is conceptually the same as the Michelson interferometer. The general scheme for a cross correlation measurement is shown in Figure 2.1. The two beams traverse separate arms of the interferometer. One of the paths has a variable length and is referred to as the delay line. The other path length is a fixed distance and serves as the reference line. By changing the length of the delay line, the time between the arrival of the delay pulse and the reference pulse at the detector can be continuously varied. Increasing the path length of the delay line causes the delay pulse to arrive at a later time with respect to the reference pulse and decreasing the path length causes the delay line pulse to arrive earlier in time. This allows the measurement of two ultrashort pulses with respect to each other, yielding a correlation function. For the case of autocorrelation, both ω_1 and ω_2 would be of the same frequency.

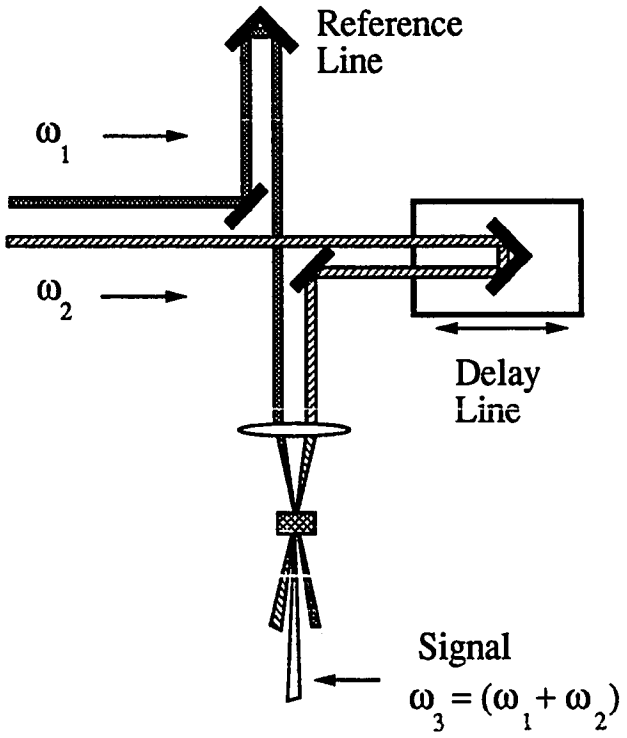

Figure 2.1: Cross correlation measurement configuration using SFM.

There are two main cross correlation detection techniques, electric field cross correlation and intensity cross correlation. Electric field correlation measures the interference between the electric fields of the delay and reference pulses. This approach may require spectral analysis due to the structure of the pulses to extract an accurate measurement [15, 16]. Intensity correlation mixes the two pulses in a medium to cause a second-order type of effect, such as SFM [14], two photon fluorescence [17], or surface SHG [18]. These processes depend only upon the intensity envelope of the pulses and are independent of the phase characteristics of the pulse.

Care must be taken relating these two correlation techniques to the associated spectra. The field correlation function is

$$g(\tau) = \int_{-\infty}^{\infty} E_1(t) E_2^*(t-\tau) dt. \tag{2.9}$$

The fourier transform of this function yields the spectral distribution, $I(\omega)$. However the intensity correlation function, given by

$$G(\tau) = \int_{-\infty}^{\infty} |E_1(t)|^2 |E_2(t+\tau)|^2 dt, \tag{2.10}$$

is the physical measurement of the pulsewidth without taking into account phase information. The fourier transform of Equation 2.10 is $I^2(\omega)$, the square of the

spectral distribution. These relationships must be taken into account when comparing measured spectra and pulsewidth correlations.

Thus an impossible measurement in time is reduced to a readily accomplished length measurement. In order to achieve femtosecond resolution, a 0.3 μm resolution would be required in the measurement of the delay line path length.

Monochromator Resolution

Measurement of the spectra of ultrashort pulses is accomplished through the use of a monochromator and is a well established process. The resolving power, **R**, for a grating monochromator is readily calculated [19] and is found to be $\mathbf{R}= \lambda/\Delta\lambda = mN$. $\Delta\lambda$ is the resolution at a central wavelength, λ. m is the diffraction order detected from the grating and N is the number of lines illuminated on the grating.

The angle described by the central maxima for diffraction from a slit of width b is:

$$\sin\theta = \frac{\lambda}{b}. \tag{2.11}$$

Likewise, the number of lines, N, illuminated on the grating can be calulated from θ using

$$\tan\theta = \frac{N/2g}{f}, \tag{2.12}$$

where f is the effective focal length of the monochromator and g is the line density of the grating in lines/mm. Solving for $\Delta\lambda$ then yields:

$$\Delta\lambda = \frac{\lambda}{2mfg\tan(\sin^{-1}(\lambda/b))}. \tag{2.13}$$

2.3 Sum Frequency Mixing of Ultrashort Pulses

2.3.1 Difficulties

Historically, methods of creating the fourth harmonic of an infrared laser, notably the Nd:YAG laser [4, 14], relied on standard SHG to double the already doubled fundamental. This method is simple and works well enough with continuous wave or long pulse lasers where pulse broadening is not a problem.

The envelope of a pulse may propagate through a medium with a different velocity than the phase of the pulse. The phase velocity v_p for a monochromatic plane wave is given as,

$$v_p = \frac{\omega}{k}. \tag{2.14}$$

The superposition of spectral components that comprise the pulse envelope move at the group velocity. The group velocity v_g is related to the index of refraction by,

$$v_g = \frac{d\omega}{dk} = \frac{c}{n - \lambda_0 \frac{dn}{d\lambda_0}}. \tag{2.15}$$

Equation 2.15 shows that the group velocity varies inversely with respect to the dispersion, $\frac{dn}{d\lambda}$. When the dispersion is nonlinear ($\frac{dn}{d\lambda} \neq constant$) the envelope will change in shape as the individual spectral components move at different velocities, resulting in a broadening of the pulse. This effect is called group velocity dispersion (GVD). In the case of normal dispersion, where the index of refraction increases with decreasing wavelength, the red components of the pulse envelope precede the blue components inducing positive chirp. Likewise, if the blue components precede the red components, the pulse is said to have negative chirp.

GVD can be compensated by the use of appropriate materials and/or geometry to introduce enough nonlinear dispersion to cancel out the chirp. But this requires additional optics, giving rise to losses from reflections and absorption, and precise knowledge of the chirp of a broadened pulse. When no chirp is present in a pulse it is considered to be transform limited, the shortest possible pulse from the given spectral components. This gives the minimum time-bandwidth product of Equation 2.7.

A problem that affects standard SHG is related to the group velocities of the fundamental frequency pulse envelope and the generated second harmonic pulse envelope. As indicated in Figure 2.2, the index of refraction changes dramatically as a function of the wavelength at the shorter wavelength end of the spectrum due to

the nonlinear dispersion. Figure 2.2 shows the index of refraction versus wavelength relation for BBO [20].

The corresponding group velocities for the fundamental and the generated second harmonic will be different though the phase velocity will be matched. This is called group velocity mismatch (GVM). Thus the pulse envelopes of the fundamental pulse and generated harmonic pulse will not continually coincide as the light propagates

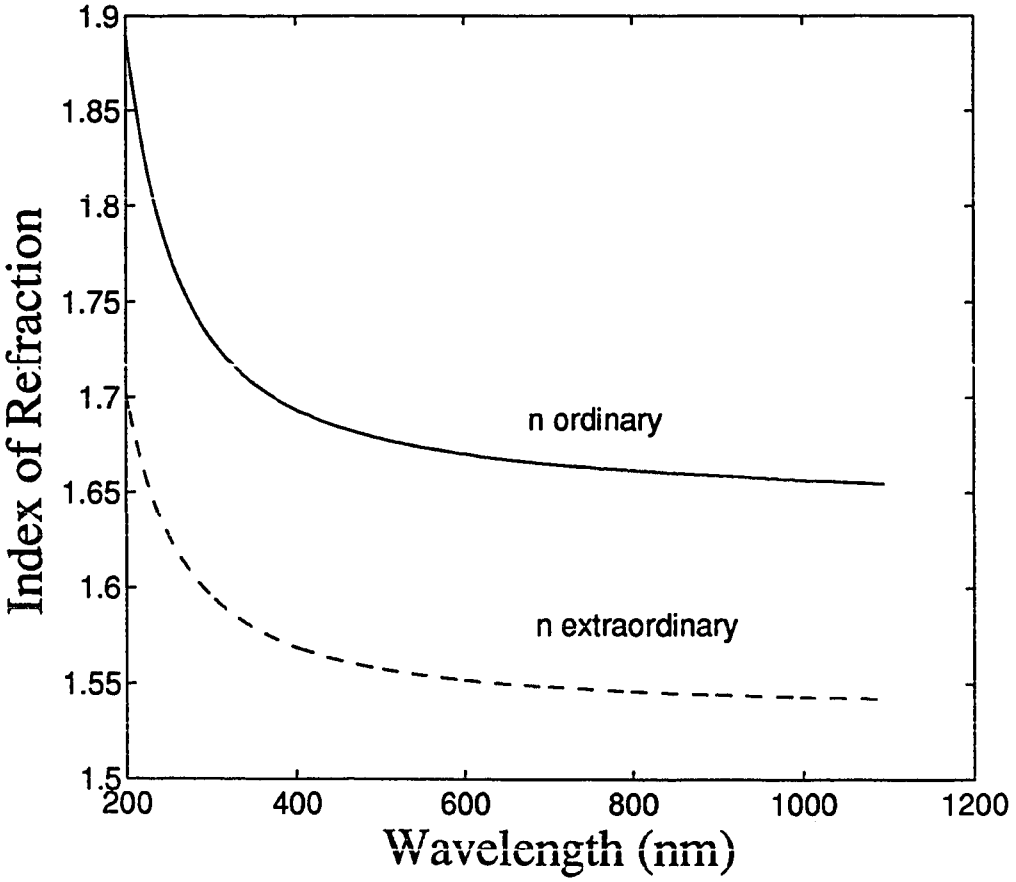

Figure 2.2: Index of refraction of BBO versus wavelength.

through the NLO crystal. In fact, the shorter wavelength second harmonic pulse will lag behind the fundamental pulse. But the fundamental pulse will continue to produce second harmonic light. This leads to a broadening of the generated second harmonic pulses and a pulsewidth longer than the fundamental pulse. GVM cannot be corrected through the use of optics in the way GVD can.

Another problem inherent to angle tuning a NLO crystal is that the wide bandwidth of the ultrashort pulse cannot be completely phase matched in a crystal by a plane wave input. The efficiency of the SFM process is determined by Δk in Equation 2.5. The orientation angle of the NLO crystal to achieve efficient phase matching is determined by the input frequencies and geometry of the mixing optics. Each configuration results in an unique phase matching angle that changes with frequency as it is derived from the dispersion of the crystal.

The spectral acceptance angle refers to the width of the spectrum that can be efficiently phase matched for a given angular input and is determined by the sensitivity of Δk to variations in the directions of the input beams with respect to the optic axis of the NLO crystal. Figure 2.3 shows the angular dependence for efficient SFM for $\omega + 3\omega = 4\omega$ in BBO as a function of the generated fourth harmonic wavelength. Note at longer wavelengths for SFM, for a given angular range, a wide spectral acceptance

is available, allowing SFM to produce ultrashort pulses. For example, given a 0.36° input angle, phase matching can occur over a 11 nm spectral range around 400 nm. This would correspond to a transform limited fundamental pulse of about 25 fs duration assuming a Gaussian distribution. However, for shorter wavelengths, the spectral acceptance across the same angular range results in a narrowed bandwidth, creating a longer third harmonic pulse since not all the input frequency components could contribute to the SFM process. The shorter wavelength fourth harmonic pulse centered at 205 nm with the same acceptance angle of 0.36° would only phase match over a 5 Å bandwidth, so the smallest pulsewidth that could be phase matched would be 125 fs, five times the minimum pulse width of the longer wavelength.

Equal angular input yields widely different ranges for possible phase matching and shows a strong dependence on the wavelength. At shorter wavelengths, the limited spectral acceptance can reduce the bandwidth of the generated sum frequency pulse and thereby lengthen the pulse in time. This is a limitation of the NLO crystal and becomes more pronounced when generating shorter wavelengths.

Associated with the concept of spectral acceptance is the angular range. The angular range refers to the cone of angles required in the crystal to phase match efficiently across the entire mixing bandwidth of the given input pulses. This is unlike

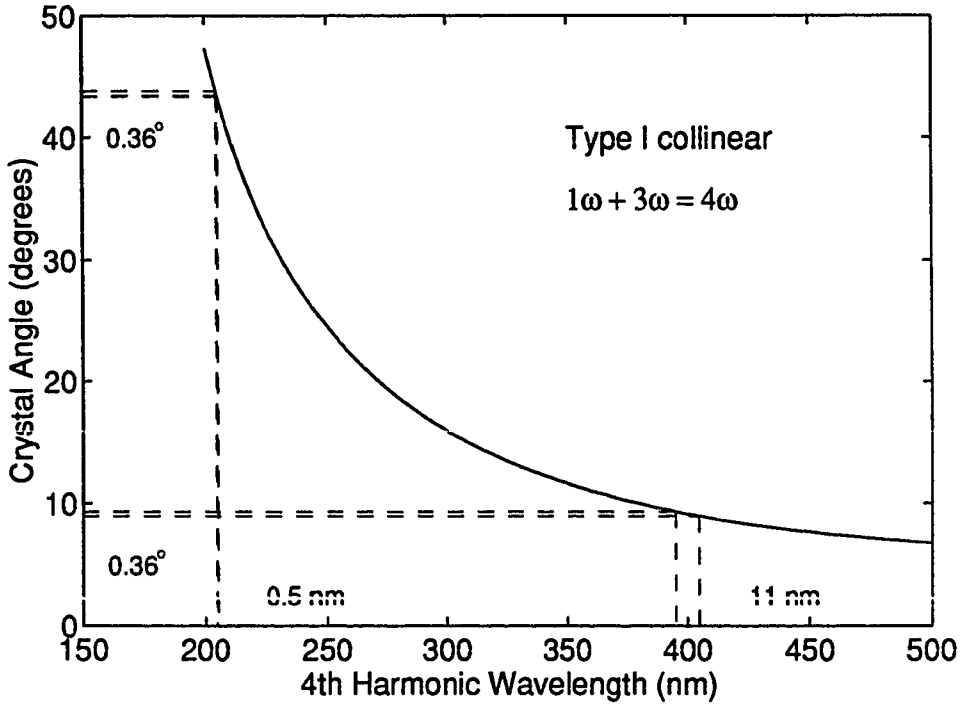

Figure 2.3: Comparison of spectral acceptances for SFM as a funtion of fourth harmonic wavelength for mixing $1\omega + 3\omega = 4\omega$. Equal angular inputs of 0.36° yield widely different ranges for possible phase matching, only 0.5 nm at 205 nm and 11 nm at 400 nm.

the somewhat misleading concept of spectral acceptance which considers the limit on the generated bandwidth for the phase matching conditions set by the crystal and the mixing geometry. Figure 2.4 shows the angular ranges for $\omega + 3\omega = 4\omega$ in BBO as a function of the generated fourth harmonic wavelength. Note at longer wavelengths for SFM, the angular range is quite small, dropping below 0.5°. Likewise, for longer pulses, the angular range decreases. The behavior of the angular range does follow the trend of the spectral acceptance by increasing sharply in the short wavelength region.

2.3.2 Solutions

Dispersive SHG and SFM have been used previously [21, 5, 22] to match the angular requirements of the SFM process. SFM for producing the fourth harmonic of an infrared laser using picosecond pulses has been reported [23, 24]. More recently fourth harmonic generation of subpicosecond near VUV (193 nm) pulses has been reported utilizing an amplified Ti:Al_2O_3 source [25].

GVD is inherent to pulses propagating through any material, however, SFM can limit the effect of broadening on the input pulses. For SFM with ultrashort pulses, the induced nonlinear polarization is only present in the crystal when both driving fields

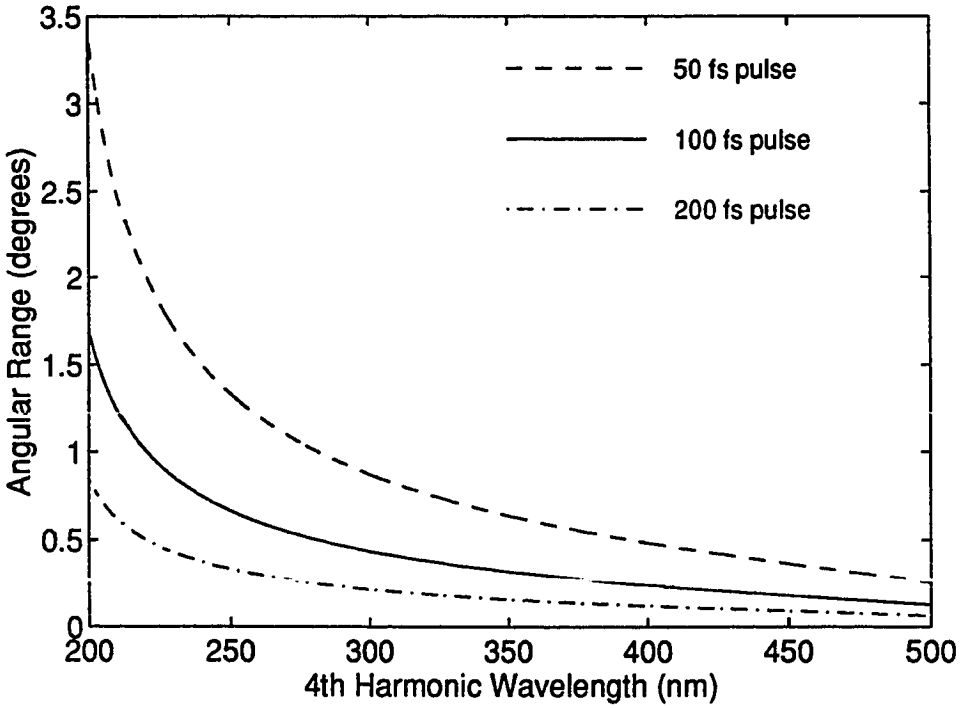

Figure 2.4: Angular range as a function of generated fourth harmonic wavelength. The ranges calculated for the bandwidths corresponding to 50 fs, 100 fs, and 200 fs pulses are shown.

are present. This means that in addition to the spatial phase matching requirements discussed earlier, the two input pulses must also be overlapping in time within the crystal to generate the sum frequency output pulse. This leads to the sum frequency pulse being generated by the superposition of a short pulse and a long pulse (refer to Equation 2.5). The short fundamental pulse preserves the ultrashort time duration.

Likewise, GVM between the input pulses and the generated sum frequency pulse will be unavoidable due to the NLO crystal. The difference in group velocities for the input pulses and the generated sum frequency pulse will only be expressed during the interaction time. Thus, unlike the situation of SHG, the sum frequency pulse is not continually generated as the input pulses propagate through the crystal.

Standard SFM counteracts pulse broadening due to GVM and GVD to some extent. Phase matching in noncollinear SFM has the extra variable of the angle between the two input beams. Proper use of this relationship can improve the spectral acceptance for SFM.

Starting from a monochromatic view, the condition for phase matching is given by $\vec{k}_1 + \vec{k}_2 = \vec{k}_3$. This is shown in Figure 2.5. Solving for the magnitude of the resultant

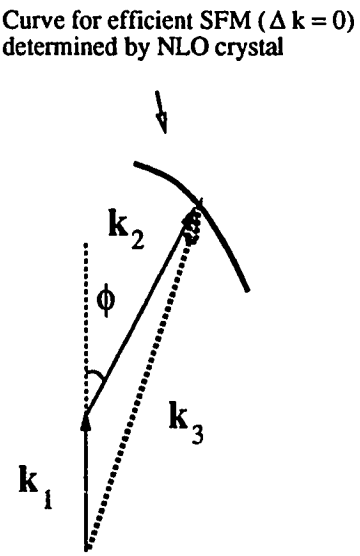

Figure 2.5: Alignment of the wave vectors in monochromatic SFM.

$\vec{k}_3$ through the use of the cosine relation yields

$$k_3 = \sqrt{k_1^2 + k_2^2 + 2k_1 k_2 \cos(\phi)}, \tag{2.16}$$

where ϕ is the angle between the fundamental, $\vec{k}_1$, and second harmonic beam, $\vec{k}_2$. If the two input beams are at the fundamental and second harmonic frequencies of the input laser, expressing this in terms of frequency and associated indices of refraction gives

$$\frac{3\omega n_3}{c} = \sqrt{\frac{\omega^2 n_1^2}{c^2} + \frac{4\omega^2 n_2^2}{c^2} + 2\frac{\omega n_1}{c}\frac{2\omega n_2}{c}\cos(\phi)}. \tag{2.17}$$

Dividing out the common terms leaves an expression for relating the indices of refraction experienced by the various harmonics:

$$n_3 = \frac{1}{3}\sqrt{n_1^2 + 4n_2^2 + 4n_1 n_2 \cos(\phi)}. \tag{2.18}$$

A similar expression is obtained for generating the fourth harmonic from mixing the fundamental and the third harmonic, yielding

$$n_4 = \frac{1}{4}\sqrt{n_1^2 + 9n_3^2 + 6n_1 n_3 \cos(\phi)}, \tag{2.19}$$

where ϕ is defined the same way as in Equation 2.16.

The angle of propagation of the sum frequency light in the crystal, θ, is determined by the angles of the two input beams. This angle is then used to determine the index of refraction experienced by a pulse at the summed frequency. This is determined by the relation for the index ellipsoid

$$\frac{1}{n^2(\theta,\omega)} = \frac{\cos^2\theta}{n_o^2(\omega)} + \frac{\sin^2\theta}{n_e^2(\omega)}, \tag{2.20}$$

where θ is measured with respect to the optic axis of the crystal.

Chapter 3

Experiment

3.1 Overview of Sum Frequency Chain

The goal of this investigation was to produce ultrashort pulses at the fourth harmonic of a Ti:Al_2O_3 infrared (IR) laser. This was accomplished through the following sequence of sum frequency generation stages:

1. Stage One: Generation of femtosecond IR pulses from the Ti:Al_2O_3 laser around 820 nm or 1.5 eV photon energies.

2. Stage Two: Second harmonic generation of the IR to produce visible/near UV pulses at 410nm or 3.0 eV.

3. Stage Three: Sum frequency mixing to produce the UV third harmonic of the Ti:Al_2O_3 laser at 273 nm or 4.5 eV.

4. Stage Four: Sum frequency mixing of the third harmonic and fundamental to produce the fourth harmonic at 205 nm or 6.0 eV.

This sum frequency chain was constructed as shown in Figure 3.1.

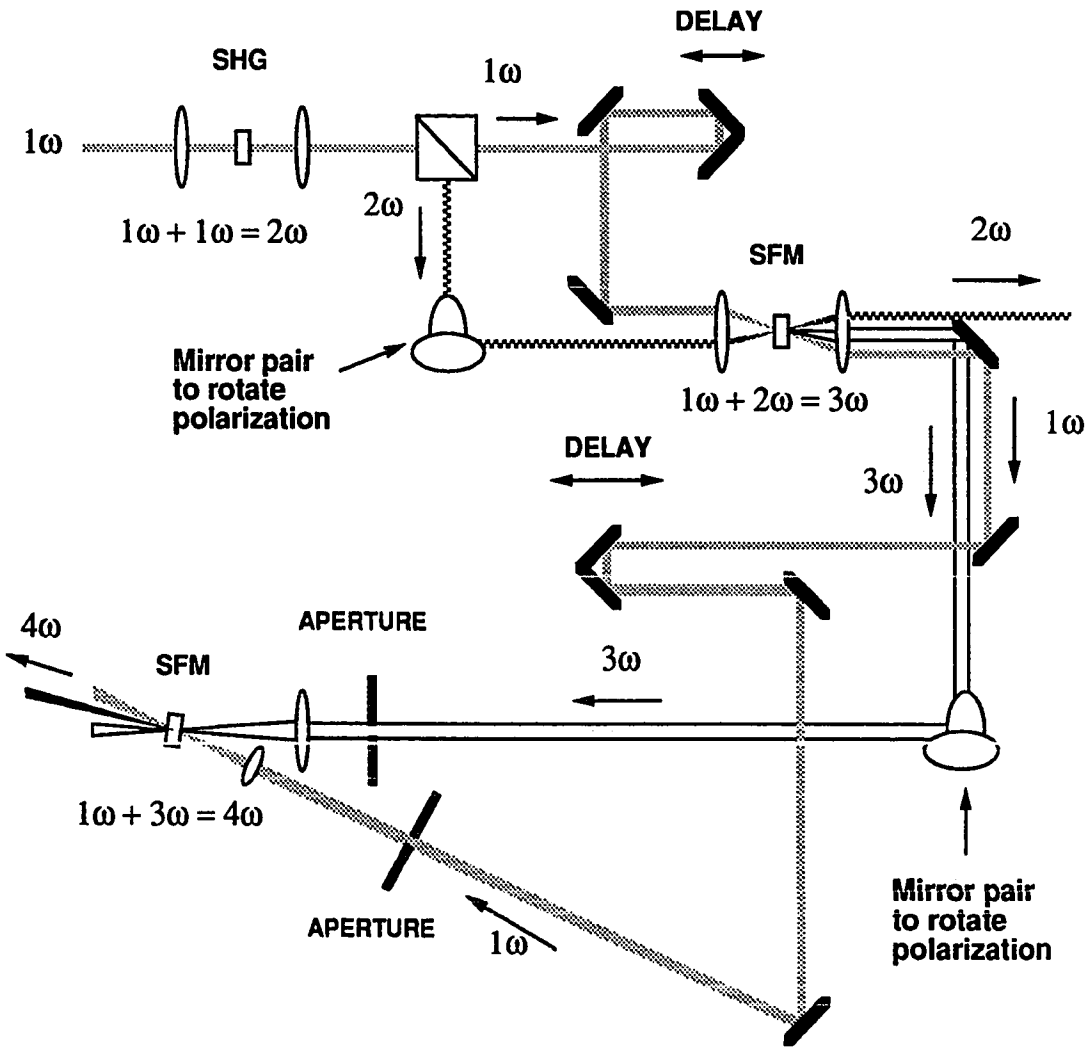

Figure 3.1: Sum frequency chain for production of fourth harmonic. The Ti:Al_2O_3 laser is not shown.

3.2 Stage One: $Ti:Al_2O_3$ Laser

The source of femtosecond laser pulses for the sum frequency chain is a Clark Instruments NJA-1 passively mode-locked titanium doped sapphire laser. This laser was assembled as shown in Figure 3.2.

The $Ti:Al_2O_3$ is pumped by a Coherent Innova Model 306 argon ion (Ar^+) laser operating in multiline mode. The recommended operating range of the Ar^+ laser was around 6 W output at open aperture resulting in a beam diameter of 1.8 mm diameter. The power of the Ar^+ laser was maintained as high as possible, usually over 7 W.

The pump laser was focused into the $Ti:Al_2O_3$ crystal gain medium. The $Ti:Al_2O_3$ laser is constructed in a linear cavity geometry. In one arm of the cavity, a prism pair introduced enough spectral dispersion to compress the chirp induced by the self

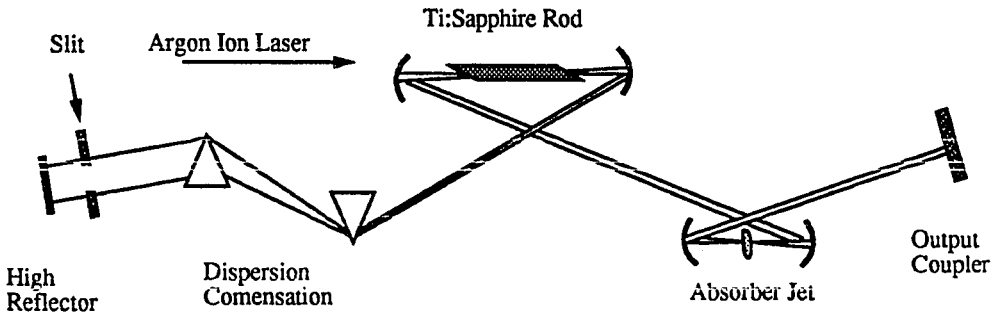

Figure 3.2: Configuration of $Ti:Al_2O_3$ laser

phase modulation that occurs in the Ti:Al_2O_3 crystal. A slit positioned before the high reflector served as a rough mechanism to select the operating wavelength and to limit the spectral content of the output.

In the other arm, a confocal spherical mirror pair in an x-configuration focused the emitted light from the gain medium through a dye jet near the output coupler. The dye jet solution consists of ethylene glycol as the solvent and small amounts of saturable absorber. The dyes used were IR-143, IR-140, and HITC. The typical concentrations were at 5 mg per dye per liter of solvent. The purpose of the absorber is to introduce a small perturbation in the cavity of the laser to help induce and maintain mode-locking resulting in stable operation [26, 27].

Mode-locking is the process where a distribution of modes occur in a resonant cavity and maintain a distinct phase relationship with the other modes. This results in the generation of short pulses as the spectral components interfere. The Ti:Al_2O_3 laser sustains mode-locking through self-focusing in the crystal [28].

Self-focusing, a manifestation of the nonlinear optical Kerr effect, occurs due to an intensity dependent term in the index of refraction of the gain medium. As the intensity increases, the index of refraction increases. The central section of the beam has a higher intensity than the marginal sections, thus experiencing a greater index

of refraction than the marginal sections. When the modes have a fixed phase relationship, the modes can interfere constructively and produce a greater intensity and a more pronounced self-focusing than under random mode operation. This focuses the beam of light into a smaller area, increasing the intensity and improving the overlap with the Ar^+ pump beam in the Ti:Al_2O_3 crystal. This improved overlap gives the mode-locked condition preferential gain and thus mode-locked operation dominates.

3.2.1 Stage One Measurements

The Ti:Al_2O_3 laser is capable of producing short pulses over an operating range of $\sim$ 750 nm to 850 nm limited by the cavity optics. Typically, the Ti:Al_2O_3 laser was operated at 820 nm in order to achieve fourth harmonic photon energies at 6 eV.

Two seperate cases are presented. In Case One, the laser source was optimized for high output power and transform limited operation. Case Two displays the performance of the sum frequency chain after maximizing the bandwidth of the Ti:Al_2O_3 laser, to make a wider range of spectra available for the SFM process, at the expense of output power. Subsequently all data presented for each case were acquired under the same operating conditions of the laser source. The spectrum of the laser output was measured with a Thermo Jarrel Ash Monospec-18 operating as a spectrometer. The

entrance slit was 50 μm. The monochromator grating was ruled at 1200 grooves/mm and blazed at 500 nm. The effective focal length of the Monospec-18 is 156 mm. Using Equation 2.13, the resolution of the spectrometer is found to be 1.3 Å. The output of the spectometer was imaged on a reticon array and relayed to a digital oscilliscope.

The intensity autocorrelation trace was measured using a Clark Instruments AC-1 autocorrelator based on the standard Michelson interferometer geometry as described in the previous chapter. The delay line had a retroreflector mounted on a speaker that oscillated at 60 Hz, sweeping through the entire scanning range. The NLO crystal was a 100 μm thick KDP crystal cut to produce the second harmonic light for a 620 nm fundamental. Some angle tuning of the KDP crystal was required to achieve a strong signal for the 820 nm light from the Ti:Al_2O_3 laser. A blue glass filter (Schott BG-28) removed the remnant fundamental light and a photomultiplier tube (PMT) served as the detector. The output of the PMT was sent to a 10 kΩ termination and was captured on the digital oscilliscope.

Case One

Figure 3.3 shows a wavelength spectrum from the Ti:Al_2O_3 laser operating under the conditions specified in Case One. The spectral width was measured to be 6.2 nm ± 1.3 Å.

The pulse measurement corresponding to the spectrum shown in Figure 3.3 is shown in Figure 3.4. The autocorrelation trace had a width of 211 fs. This corresponds to a 159 fs pulse width, assuming a Gaussian distribution.

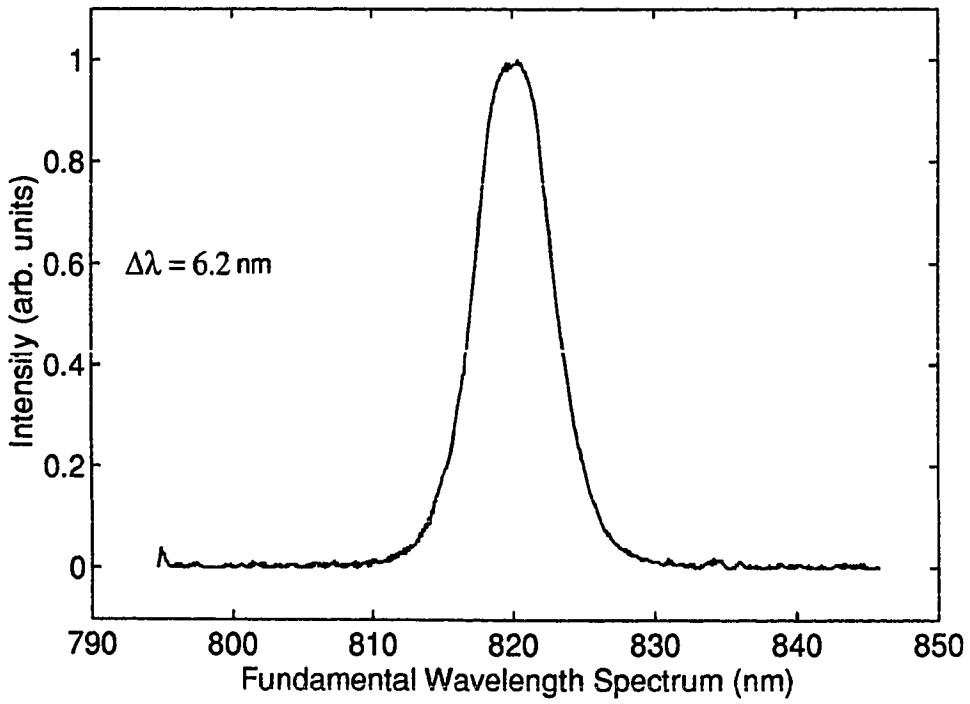

Figure 3.3: Case One: Spectrum of the fundamental IR pulse. The resolution of the spectrometer was 1.3 Å.

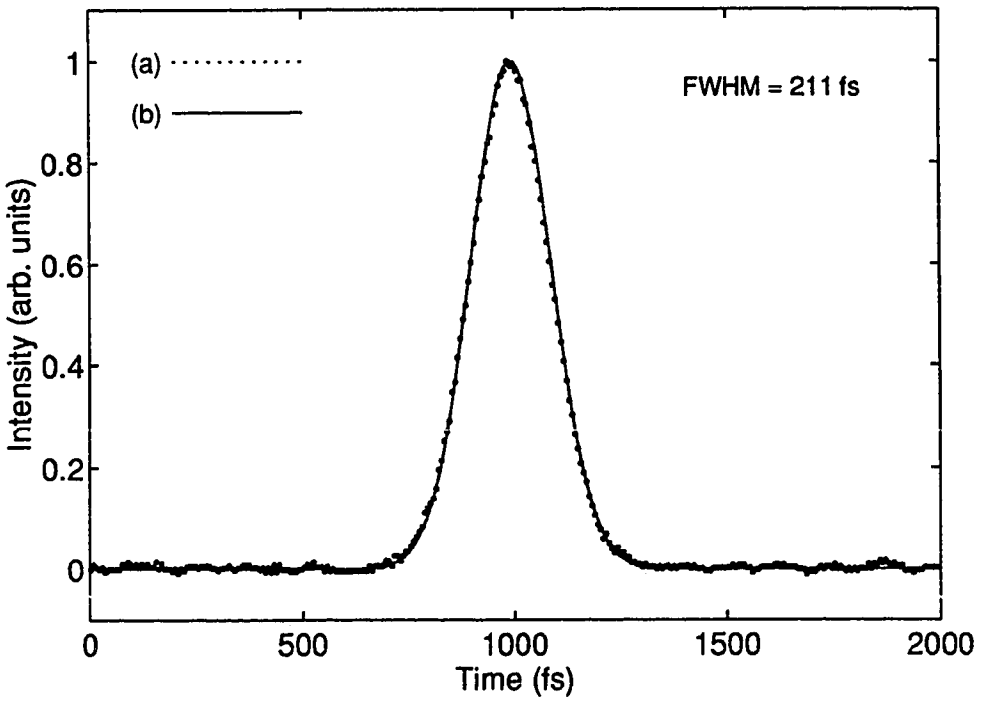

Figure 3.4: Case One: Autocorrelation trace of the fundamental IR pulse. The dotted line(a) shows the AC measurement with a 211 fs FWHM. The solid line(b) shows the fit to the autocorrelation of a Gaussian pulse of 159 fs width.

Fundamental Pulse Broadening Through Sum Frequency Chain

As the fundamental pulse is used to make all subsequent pulsewidth measurements through cross correlations of the generated sum frequency pulses as well as serving as a limiting factor of the pulsewidth in the fourth harmonic stage, the question of broadening of the fundamental pulse must be considered. Thus several autocorrelation measurements were performed at points along the sum frequency chain. Both the temporal and spectral characteristics of the fundamental beam were measured after the initial generation of the infrared light after Stage One, after the second harmonic generation in Stage Two, and after the SFM in Stage Three.

The same autocorrelator was used for each measurement. Some broadening due to the dispersion found in refractive optics was observed as shown in Figure 3.5, but the effect was relatively minor for pulses of $\sim$ 159 fs. The results of the measurement are contained in Table 3.2.1. Each pulse was fitted to a Gaussian type distribution and the given temporal widths are for the electric field of the fitted pulse.

Case Two

Figure 3.6 shows the wavelength spectrum of the Ti:Al_2O_3 laser output for Case Two with a broad output spectrum, obtained by changing the alignment of the cavity. This

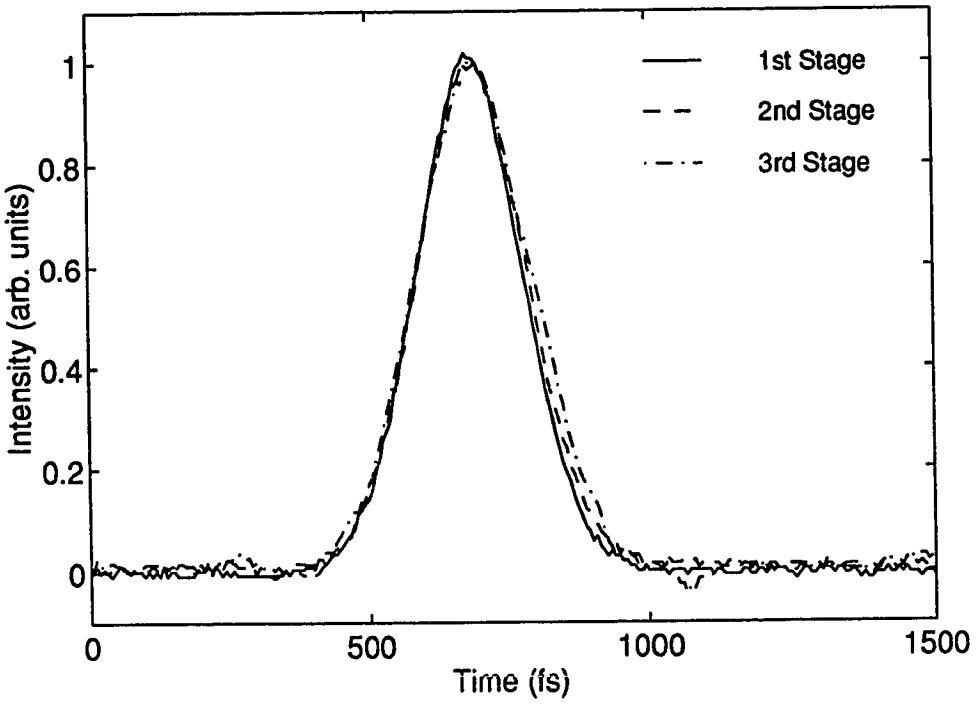

Figure 3.5: Comparison of autocorrelation traces for the fundamental beam at three points in the sum frequency chain.

Location	Δt	$\Delta\nu\Delta t$
First Stage	159 fs	0.44
Second Stage	164 fs	0.579
Third Stage	172 fs	0.583

Table 3.1: Measurement results for fundamental pulse deformation through sum frequency chain.

modification of the laser output was done in order to increase the spectra available to produce the sum frequency light to test the effect of an enhanced input bandwidth. The spectral width was measured at 13.9 nm ± 1.3 Å.

In Figure 3.7, the corresponding autocorrelation trace for the pulse output of Figure 3.6 is shown. The width of the autocorrelation trace was found to be 180 fs which corresponded to a 129 fs pulse width assuming a Gaussian fit. Both measurements were made using the same methods and equipment as Case One.

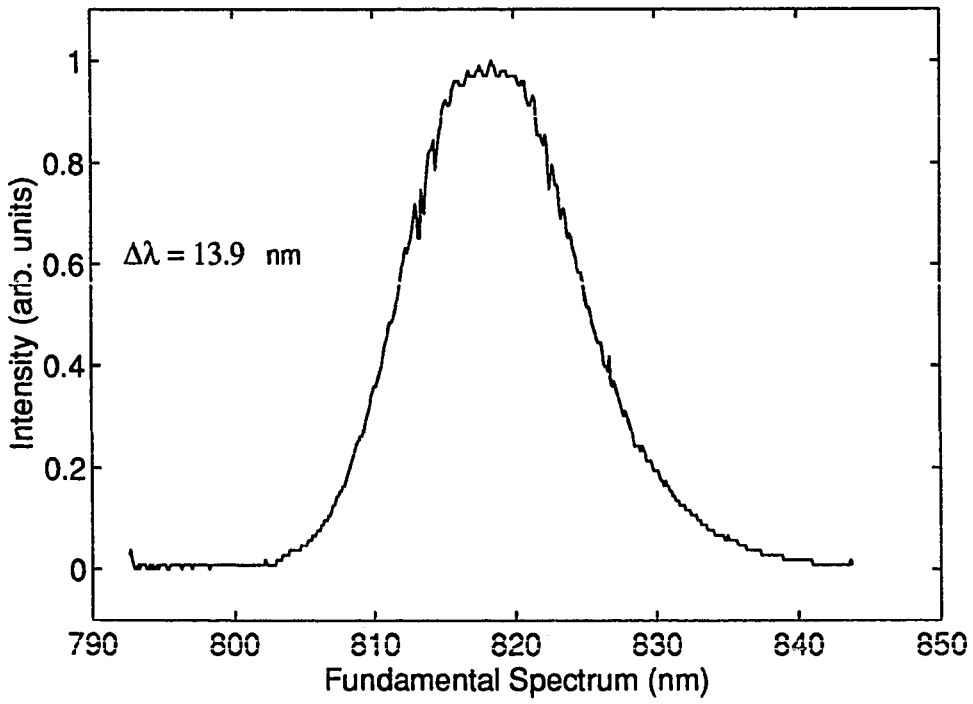

Figure 3.6: Case Two: Spectrum of the fundamental IR pulse. The resolution of the spectrometer was 1.3 Å.

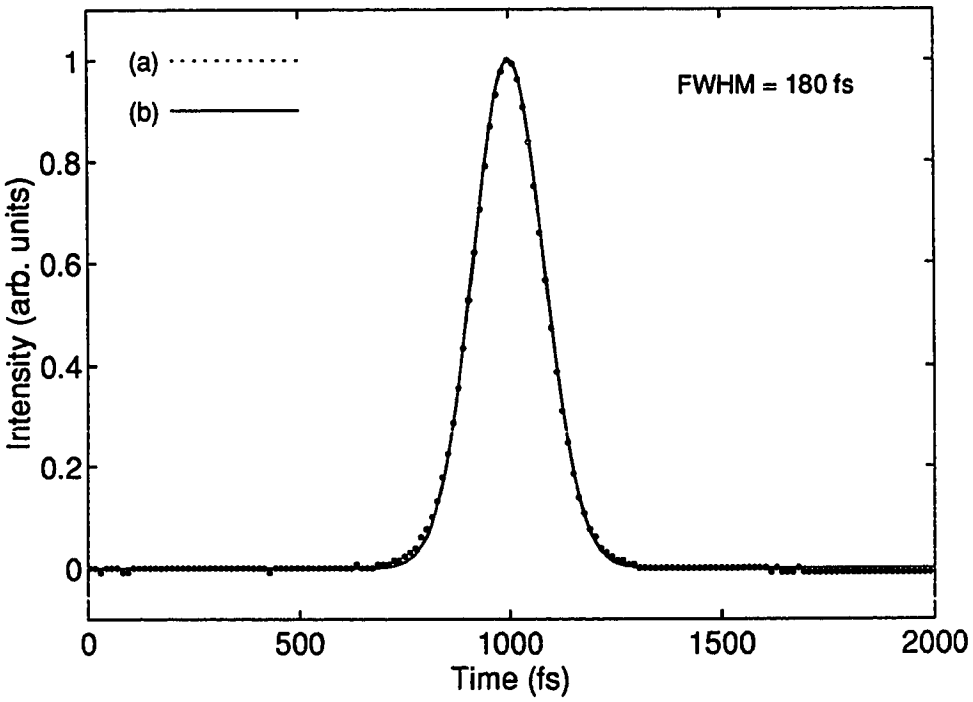

Figure 3.7: Case Two: Autocorrelation trace of the fundamental IR pulse. The dotted line (a) shows the AC measurement with a 180 fs FWHM. The solid line (b) shows the fit to the autocorrelation of a Gaussian pulse of 129 fs width.

Table 3.2.1 contains the electric field pulse widths corresponding to the intensity autocorrelation traces presented for both Case One and Case Two. The electric fields are assumed Gaussian distributions. The power was measured with a Newport Model 835 power meter. Along with typical power output and spectral widths, the time-bandwidth product is shown.

3.3 Stage Two: Second Harmonic Generation

After the femtosecond pulses are produced in the Ti:Al_2O_3 laser, the pulses are passed through an Electro-Optics Technology 1845 Series faraday isolator. The faraday isolator prevents external feedback into the laser cavity that can disrupt the mode-locked operation. The faraday isolator rotates the polarization of the IR pulses 90° such that it is perpendicular to the surface of the optical table.

	Case 1	Case 2
Power (cw)	230 mW	180 mW
Δt	159 fs	129 fs
$\Delta\lambda$	6.2 nm	13.9 nm
$\Delta t \Delta\nu$	0.44	0.80
× transform limit	1.0	1.8

Table 3.2: Characteristics of the Ti:Al_2O_3 output.

Once through the isolator, the IR pulses at 820 nm are frequency doubled using standard SHG. This is shown in Figure 3.8. The crystal used here is a 1.5 mm thick lithium borate (LBO) crystal. The LBO, a biaxial crystal, was cut at 90° with respect to the z optic axis and 27° with respect to the x optic axis [29]. LBO was chosen over BBO for the second stage due to the superior beam profile of the generated second harmonic. Any decrease in beam quality causes decreased conversion efficiency further down the sum frequency chain. LBO has a walk-off angle of $\approx 1°$ compared to BBO with a walk-off of 39° at this fundamental frequency [23].

The second stage produces light in the blue-violet end of the visible spectrum at 410 nm for an 820 nm fundamental wavelength.

3.3.1 Stage Two Measurements

The spectra of the second harmonic light were measured with a Thermo Jarrel Ash Monospec-18 operating as a monochromator fitted with a 2400 grooves/mm diffraction grating blazed for 250 nm light. The entrance and exit slits were 100 μm and 50 μm wide respectively. The resolution of the monochromator is found to be 1.3 Å from Equation 2.13.The detector was a Hamamatsu R928 PMT.

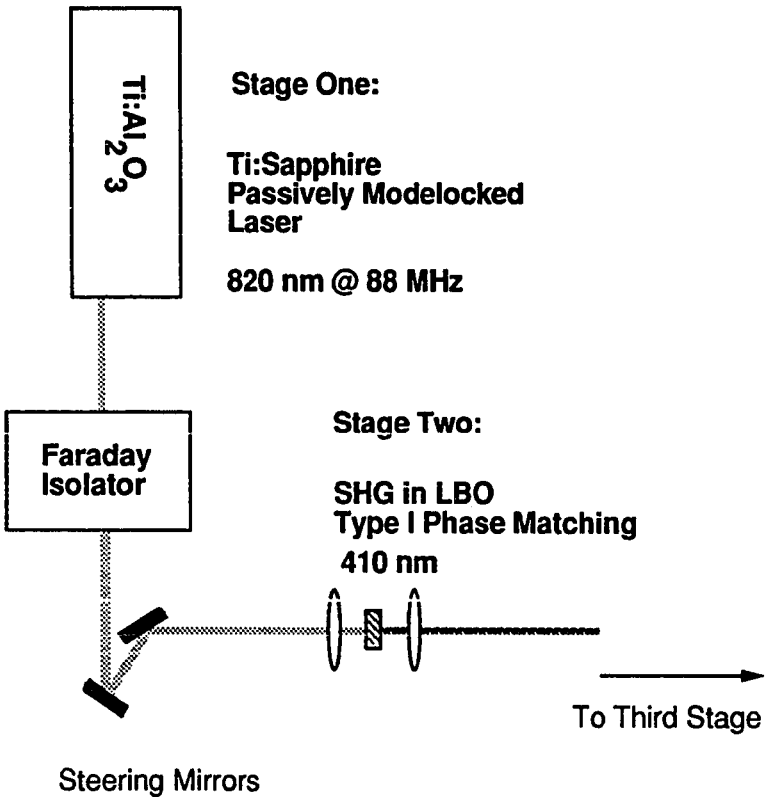

Figure 3.8: Stage One and Two of the sum frequency chain

The pulsewidth measurements were made through a cross correlation scheme by using the delay line in Stage Three to move the fundamental pulse in time with respect to the second harmonic pulse train. The fundamental and second harmonic pulses interacted to produce pulses at the sum of their frequencies. A more detailed description of this process follows in Section 3.5.

Case One

The corresponding spectral distribution and cross correlation trace for Case One as presented in the first section follow. The maximum continuous output power achieved was around 15 mW, however 12 mW was the typical operating range for the case of a longer pulse. The spectral width was measured at 2.3 nm $\pm$ 1.3 Åand the cross correlation trace had a width of 316 fs. The pulse would then fit to 284 fs pulse assuming a Gaussian distribution correlated with the known fundamental pulse shape. The observed broadening in the pulse width is due to GVD within the calcite of the polarizing beamsplitter used to separate the fundamental and second harmonic beams in Stage Three.

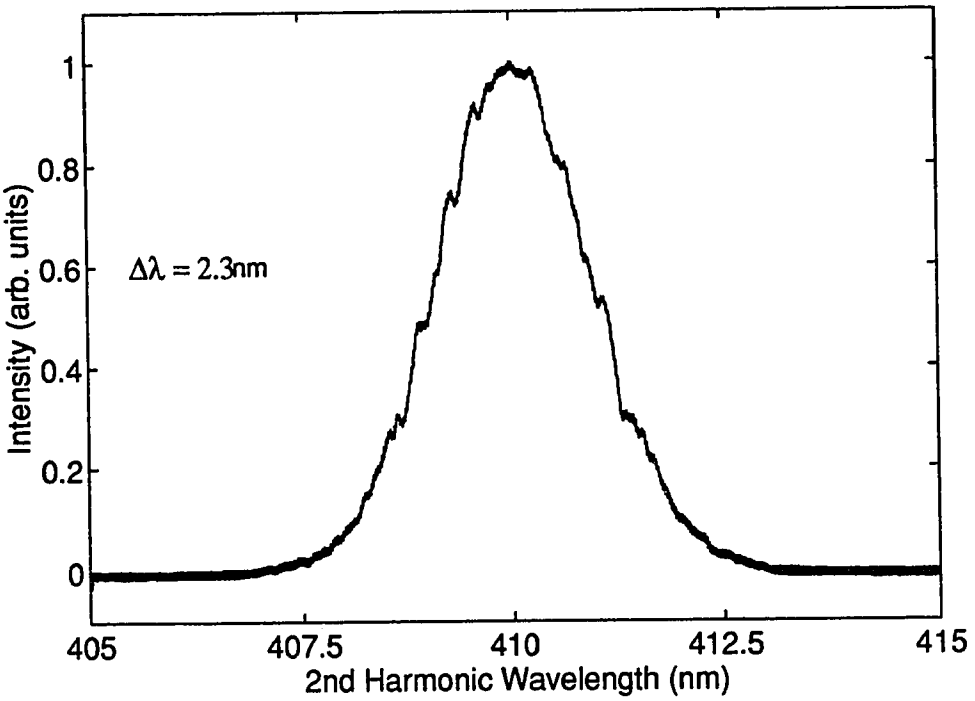

Figure 3.9: Case One: Spectrum of the second harmonic pulse

Case Two

The following spectral and pulsewidth measurements for Case Two are the average of four individual measurements. The spectral width was measured at 4.2 nm ± 1.3 Å. The cross correlation trace yielded a FWHM of 345 fs which corresponds to a pulsewidth of 310 fs when using the known fundamental for reference. Gaussian distributions are assumed. The deviation from the fit near the trailing edge of the cross correlation trace indicates a slight asymmetry in the second harmonic pulse.

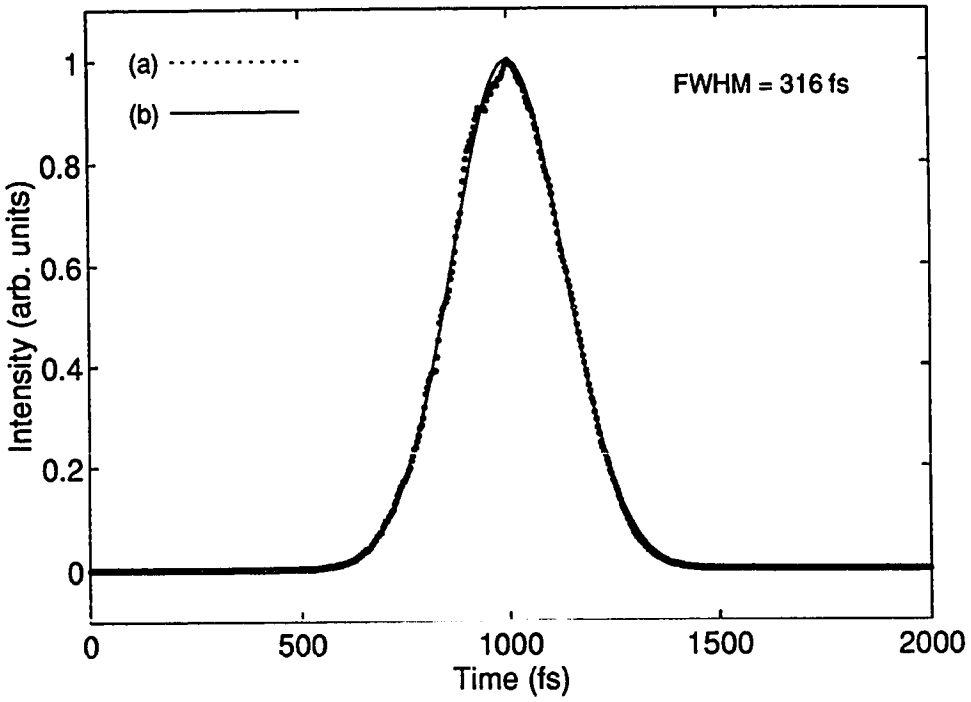

Figure 3.10: Case One: Intensity cross correlation of the second harmonic and fundamental using the crystal in Stage Three. The dotted line (a) shows the cross correlation measurement with a 316 fs FWHM. The solid line (b) shows the fit to the cross correlation of a Gaussian pulse of 284 fs width with the previously determined fundamental pulse shape.

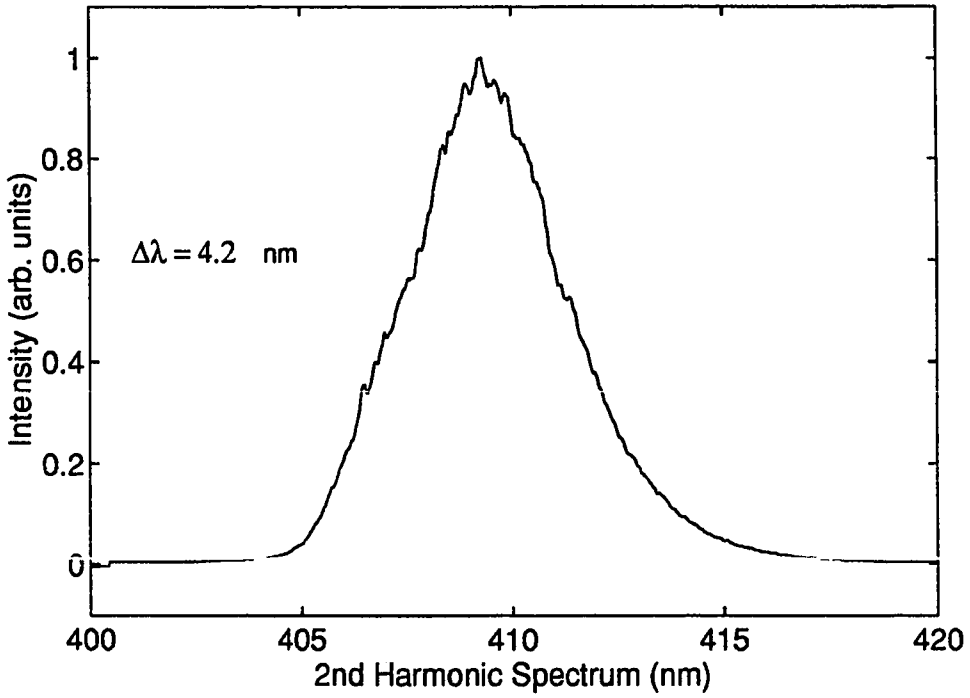

Figure 3.11: Case Two: Spectrum of the second harmonic pulse. The resolution of the monochromator is 1.3 Å.

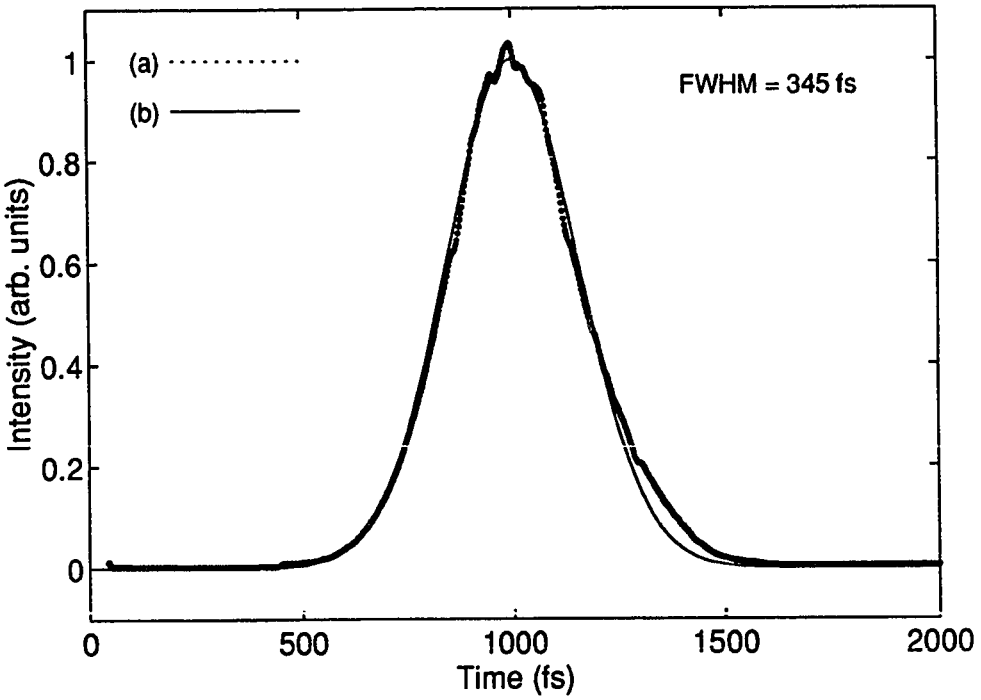

Figure 3.12: Case Two: Cross correlation of second harmonic and fundamental in Stage Three. The dotted line (a) shows the cross correlation measurement with a 345 fs FWHM. The solid line (b) shows the fit to the cross correlation of a Gaussian pulse of 310 fs width with the known fundamental pulse shape.

Table 3.3.1 contains the measurement results for the second harmonic output of the second stage of the sum frequency chain. The power measurements given are the powers measured directly before the subsequent stage in the sum frequency chain.

3.4 Stage Three: Third Harmonic SFM

The third stage is shown in Figure 3.13. The IR fundamental beam and the blue second harmonic propagate collinearly after the second stage. The first element in the third stage is a Thompson polarizing beam splitter. This particular type of beam splitter was chosen for the absense of angular dispersion and low absorption.

Once the beams are separated, the second harmonic beam is reflected from a pair of mirrors that are mounted at 45° with respect to the surface normal of the table. The direction of propagation is redirected 90° from the previous direction of propagation which rotates the optical polarization of the second harmonic beam 90° such that it

	Case 1	Case 2
Power (cw)	12 mW	8 mW
Δt	284 fs	310 fs
$\Delta\lambda$	2.3 nm	4.2 nm
$\Delta t\Delta\nu$	1.15	2.4
× transform limit	2.6	5

Table 3.3: Characteristics of the second harmonic output.

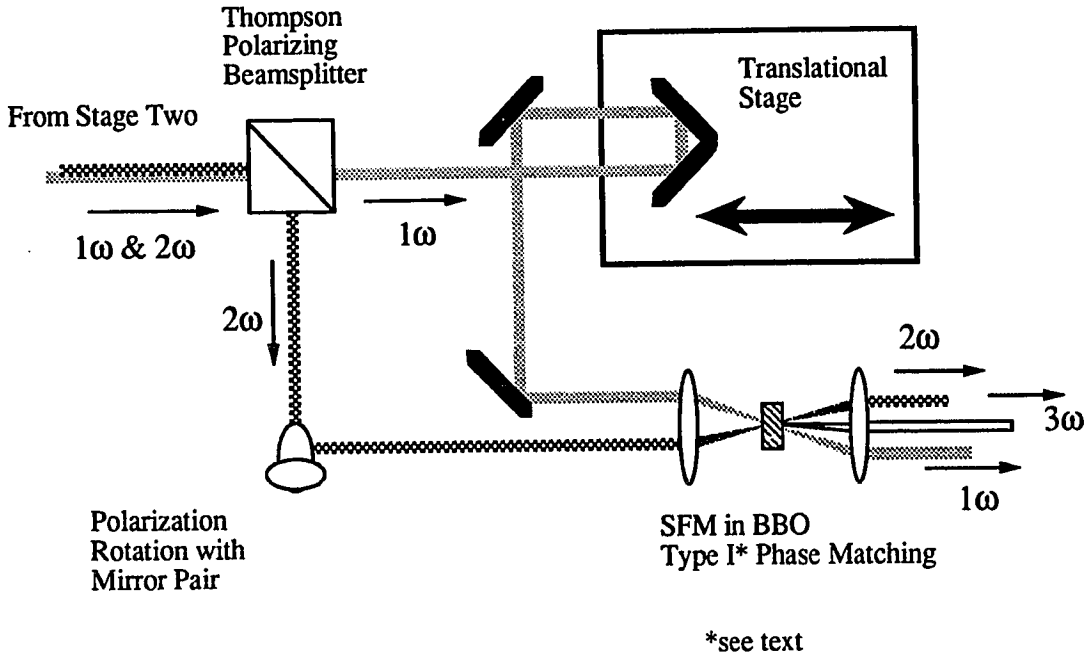

Figure 3.13: Stage Three: Noncollinear SFM for producing the third harmonic.

has the same polarization as the fundamental beam. This is done to allow Type I phase matching where the two input beams share a common polarization along the ordinary axis of the NLO crystal. The generated sum frequency light will then be polarized along the extraordinary axis of the crystal, orthogonal to the input beams. Due to the orientation of the beamsplitter and the use of a mirror pair to change the polarization, the second harmonic beam is vertically displaced about 5 mm below the IR beam.

The fundamental beam passes through a delay line to compensate for path length differences incurred through the SHG and pulse separation processes. This delay line also allow the cross correlation measurement for determining the temporal pulse width of the second harmonic beam.

At this point, both beams are passed through a 50 mm focal length achromat and focused into a 1 mm thick BBO crystal. The vertical distance between the two input beams was $\approx$ 4 mm, well within the paraxial regime for the achromat. The third stage BBO crystal was cut at 37° with respect to the optic axis. The third harmonic UV light is generated through noncollinear SFM when the input fundamental and second harmonic pulses are properly aligned.

3.4.1 Variation of Noncollinear Sum Frequency Mixing Geometry

Two distinct orientations exist for noncollinear Type I SFM phase matching. This is shown in Figure 3.14. Figure 3.14 (a) corresponds to the most common configuration where both input beams propagate in a plane perpendicular to their colinear electric field polarization. This is a plane described by an ordinary and the extraordinary axis of the biaxial crystal. In the other configuration, Figure 3.14 (b), the wave vectors propagate in a plane, but the polarizations are not parallel. So the plane containing

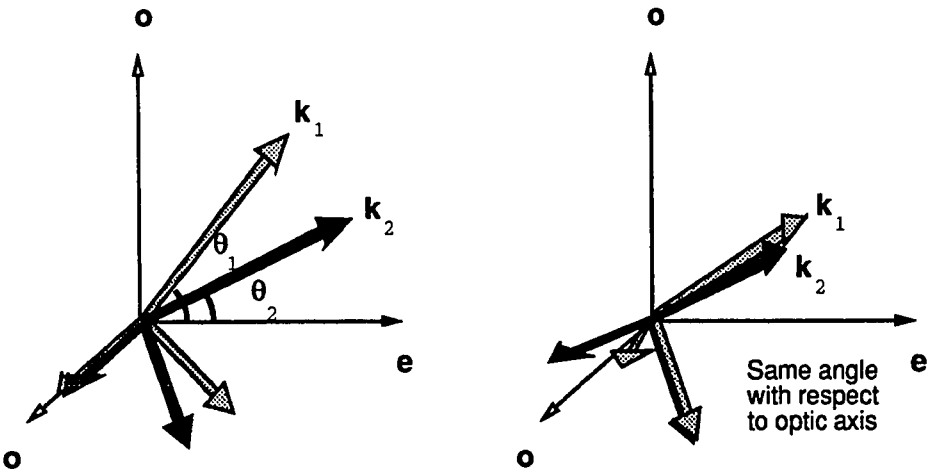

Figure 3.14: Two variations of SFM

the wavevectors lies perpendicular to the plane of the ordinary and extraordinary axes.

The nonlinear coefficients which determine d_{eff} have a weak frequency dependence in the visible and near UV range [20]. The effective nonlinear coefficient is dependent upon the angle of propagation in the crystal. The angle between the fundamental and the second harmonic for this third harmonic generation was 5°. This angle is small enough that no effective change is predicted in the nonlinear coefficient. For nearly collinear SFM these two configurations are equivalent.

3.4.2 Timing Alignment

Alignment of the third stage to match the delay line of the IR beam to the path length of the second harmonic beam so both pulses would coincide in the mixing crystal followed an iterative process. SFM is used to produce maximal temporal and spatial overlap in the BBO crystal.

First, a 50 μm pinhole was positioned such that the beam waist of the second harmonic pulse passed through it. Then the fundamental beam waist was steered to pass through the pinhole. A fast p-i-n photodiode was placed in the focal region for both beams and a rough timing signal was found on a Tektronix 7104 sampling scope. By adjusting the delay line the fundamental pulse could be placed within 10 ps of the blue pulse, corresponding to about 3 mm of path length in the delay line.

Once the rough timing was done, a Hamamatsu R166 solar blind photomultiplier tube (PMT) was placed near the output of the BBO crystal. The Cs-Te photocathode material has a limited spectral sensitivity, from 160 nm to 320 nm. Thus it is insensitive to both the fundamental and second harmonic wavelengths. A mechanical chopper was placed in the fundamental line to modulate the IR beam. The delay line was translated across the range determined by the rough timing and the orientation

of the BBO was changed. The reflections from the face of the crystal were used to determine the angle of the input beams.

The output of the PMT was amplified and filtered using a Stanford Research Systems SR560 filtering preamplifier. The bandpass filter of the SR560 was centered on the chopping frequency, around 2 kHz. The typical preamplifier gain was set to 50. The filtered signal was then detected by a Stanford Research Systems SR850 lock-in amplifier.

The delay line was moved until a signal from the generated third harmonic light at 273 nm was detected by the solar blind PMT. The intense fundamental beam was blocked from the PMT to prevent thermionic emissions from the photocathode due to the repetitive heating from the chopped IR beam. Once a signal from the generated sum frequency light was detected, the power of the output was increased by optimizing the BBO angle, the position of the BBO in the focus, the delay line path length, and beam paths through careful iteration.

3.4.3 Stage Three Measurements

The spectra of the third harmonic light was measured with a Monospec-18 fitted with a 2400 grooves/mm diffraction grating, and the solar blind PMT served as the

detector. The entrance and exit slits were 100 μm and 50 μm respectively yielding a resolution of 1.3 Å. The cross correlation of the third harmonic pulse with the fundamental pulse was performed in Stage Four by changing the path length of the delay line. All measurements were taken with the generated third harmonic sum frequency light optimized for power.

Case One

Figure 3.15 shows the spectra for Case One. Figure 3.16 shows the matching cross correlation measurement. The highest power measured for the third harmonic light was 225 μW. However, the best power available for the following fourth harmonic SFM stage was around 100 μW due to reflections and lossy mirrors. The spectral width was measured to be 9.5 Å $\pm$ 1.3 Å. The cross correlation trace yielded a width of 396 fs. When fitted to the known fundamental, the pulsewidth matched a 366 fs pulse. This increased pulse width is due to the compounded effects of GVM in the 1 mm long crystal, GVD in the crystal and through the fused silica focusing lenses before the correlation measurement, and phase matching contstraints.

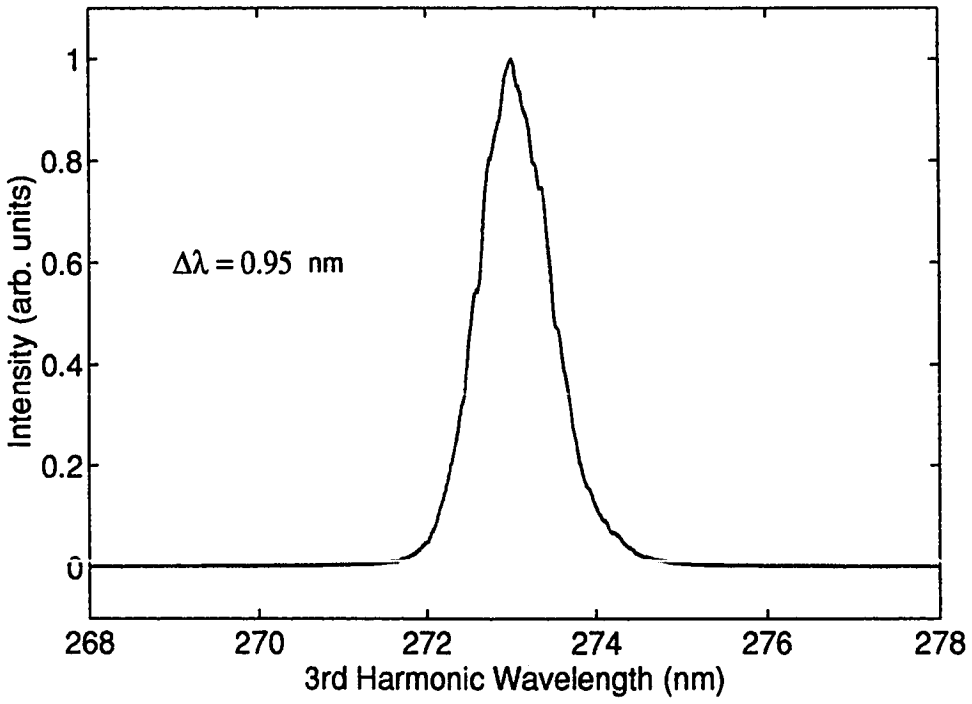

Figure 3.15: Case One: Spectrum of the third harmonic pulse measured with a resolution of 1.3 Å.

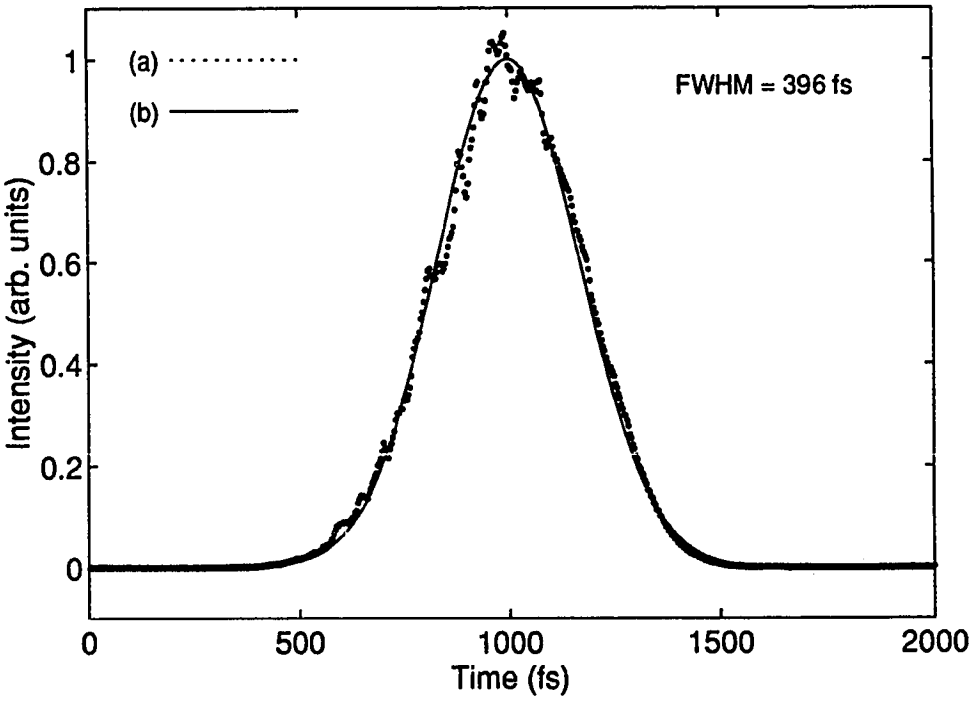

Figure 3.16: Case One: Cross correlation of third harmonic and fundamental in Stage Four. The dotted line (a) shows the cross correlation measurement with a 396 fs FWHM. The solid line (b) shows the fit to the cross correlation of a Gaussian pulse of 366 fs width with the known fundamental pulse shape.

Case Two

Figure 3.17 shows the spectrum of the third harmonic in Case Two averaged over four measurements. Figure 3.18 shows the cross correlation trace for the third harmonic averaged over three measurements for the same conditions. The input fundamental power for this stage was around 110 mW. The spectrum had a measured 1.47 nm $\pm$ 1.3 Åwidth and a cross correlation width of 531 fs. A 500 fs pulse would produce a cross correlation with the known fundamental to match the measured correlation trace. The broad pulse width measured is expected from GVM through the 1 mm long BBO crystal, GVD in the crystal and focusing lenses, and phase mismatch to a greater extent than Case One due to the broader bandwidths of Case Two.

Table 3.4.3 lists the characteristics of the third harmonic output. The powers given are the powers available for SFM in the next stage.

	Case 1	Case 2
Power (cw)	100 μW	25 μW
Δt	366 fs	500 fs
$\Delta\lambda$	0.95 nm	1.47 nm
$\Delta t\Delta\nu$	1.4	3.0
$\times$ transform limit	3.2	7.3

Table 3.4: Characteristics of the third harmonic output.

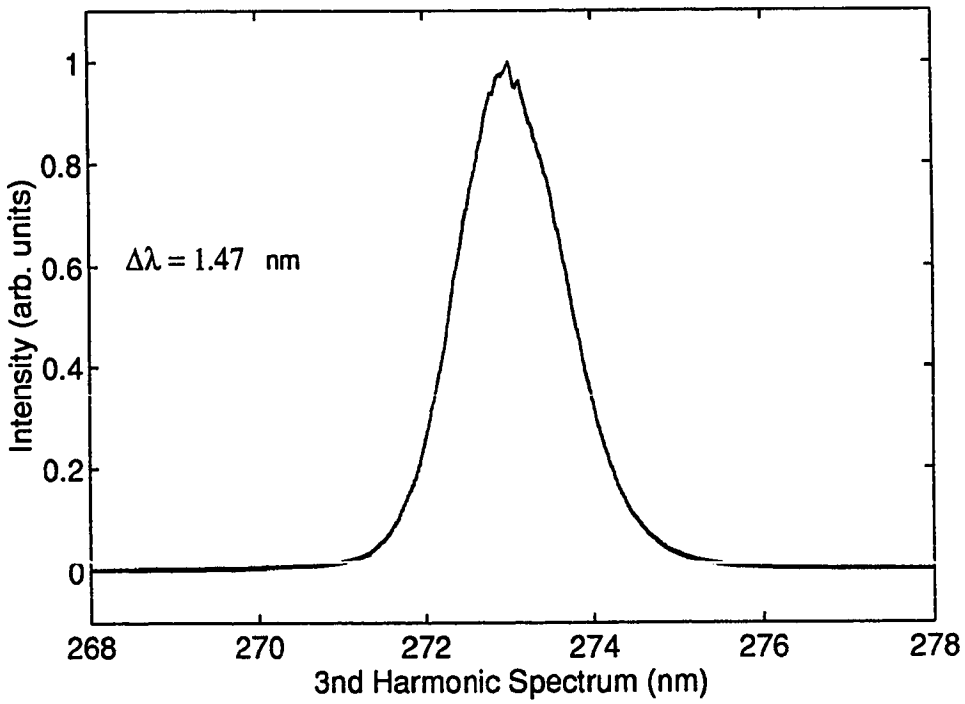

Figure 3.17: Case Two: Spectrum of the third harmonic pulse. The resolution is 1.3 Å.

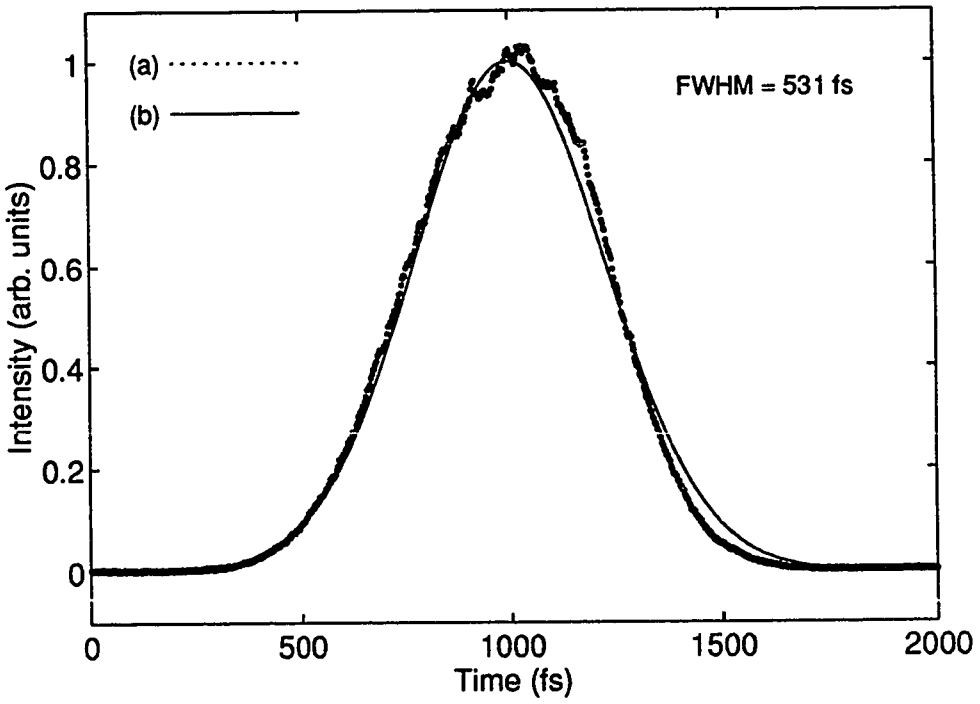

Figure 3.18: Case Two: Cross correlation of third harmonic and fundamental in Stage Four. The dotted line (a) shows the cross correlation measurement with a 531 fs FWHM. The solid line (b) shows the fit to the autocorrelation of a Gaussian pulse of 500 fs width.

3.5 Stage Four: Fourth Harmonic SFM

In the final stage of the sum frequency chain, the blue second harmonic light is discarded. As the IR fundamental and UV third harmonic beams are spatially separated, mirrors are used to redirect the beam paths. Figure 3.19 shows the last stage.

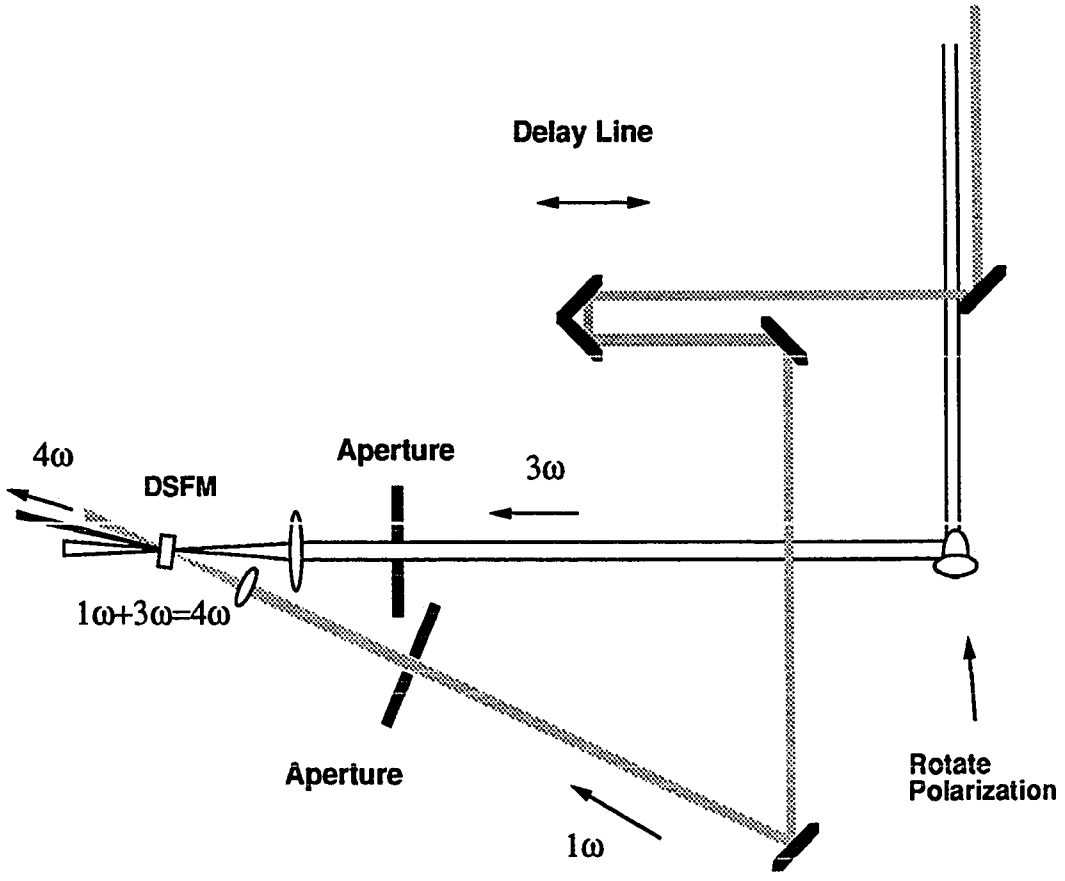

Figure 3.19: Stage Four: Noncollinear SFM for the production of the fourth harmonic.

The third harmonic beam passes through another mirror pair to rotate the polarization such that it is parallel with the IR fundamental beam. The third harmonic beam is raised to the same height as the fundamental beam.

The fundamental beam again passes through a delay line and is focused into the mixing BBO crystal with a 25 mm focal length lens. The third harmonic beam is focused into the crystal with a 50 mm focal length quartz lens. This is in order to match beam waists of the radically different frequencies. The focal spot sizes for the fundamental and third harmonic beams would then be 6.5 μm and 8.6 μm respectively in the diffraction limit.

The angle ϕ between the fundamental and third harmonic beams was $\approx 20°$. Beam and lens diameters determined the geometry, limiting how small ϕ could be constructed.

The orientation of the fundamental beam with the BBO crystal was at $\approx 15°$ with respect to the surface normal. The BBO was cut at 67° with respect to the optic axis according to the manufacturer. The thickness of the BBO was chosen to correspond to the distance where GVD would cause the generated fourth harmonic pulse to be delayed by one pulse width, taken to be 150 fs, behind the IR fundamental pulse. This resulted in a 100 μm thick BBO crystal matching the requirements.

3.5.1 Timing

Positioning the beam paths to coincide within the few microns that describe the spatial extent of femtosecond laser pulses raises interesting problems. In the third stage, both the fundamental and second harmonic beams were energetic enough to time the pulses using SFM with relatively poor alignment. Detection was readily made in the third stage as the solar blind PMT was sensitive to the third harmonic at 273.3 nm, and was insensitive to the 410 nm and 820 nm light. However the fourth harmonic light at 205 nm falls within the detection range of the PMT as well as scattered third harmonic light.

Two lenses are used for the focusing of the input beams increasing the variables for pulse overlap in space. Rough timing with the p-i-n photodiodes cannot be made with an accuracy of more than 50 ps due to the low sensitivity of the diode to the third harmonic wavelengths.

In order to align the pulses in time, another approach was required. Transient bleaching in a dye jet proved an ideal method for finding temporal pulse overlap. IR132 dye proved to have two strong absorption bands centered at 820 nm and 270 nm. In IR132, the IR absorbance is nearly 4 times the UV absorbance. This fortuitous

occurance provided the mechanism for detecting the overlap of the fundamental and third harmonic pulses in time and space.

As depicted in Figure 3.20, absorption of photons takes electrons to higher energy states. If the ground level is depopulated, no absorption can take place until the ground state is repopulated by decaying excited states. The relative intensity of the IR is higher than the UV by 3 orders of magnitude, corresponding to a photon ratio of 3000:1 in favor of the IR.

The intense fundamental pulse depopulates the ground state of the IR132 molecule, and allows transmission of the third harmonic pulse. However, the lifetime of the first excited states in IR132 must be less than a few nanoseconds in order to function as

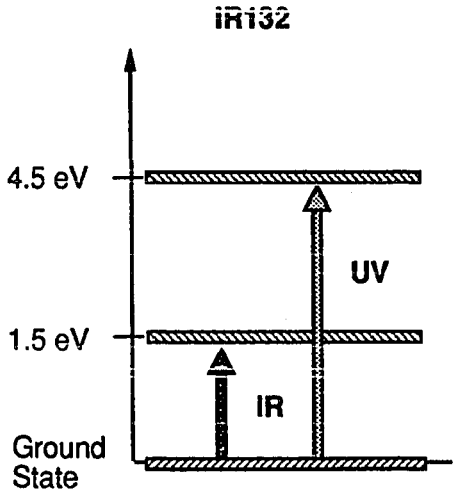

Figure 3.20: Prominent absorption energy levels in IR132 dye.

a laser dye. Since the Ti:Al_2O_3 laser operates at 87 MHz, there is about a ten nanosecond period between successive pulses, enough time for the IR132 molecules to relax back into the ground state. Thus a sudden change in transmission of the UV light is expected around the point where the third harmonic and fundamental pulses temporally coincide in the dye.

This measurement was made by substituting a dye jet for the NLO crystal shown in Figure 3.19. The dye concentration in the ethylene glycol solvent was increased to the point where $\sim$ 50% of the IR beam was absorbed.

Differential detection was utilized to reduce the noise contribution from fluctuations in the source laser. Reflected third harmonic light from the first prism was detected with a photodiode and served as a reference signal. The transmitted third harmonic light was collected on another photodiode after passing through a Schott Glass UG-11 filter to remove stray IR light. The two signals from the photodiodes were compared and subtracted in the preamplifier and the reference signal strength was modfied with a variable attenuator to minimize the noise contribution. The preamplifier gain was typically set to 5000 with two 10 kΩ terminations. The fundamental beam was modulated with a mechanical chopper, operating at 2 kHz frequency. The signal from the preamplifier went to the lock-in amplifier.

The two spots in the dye were roughly aligned through the use of a stereo microscope until a signal was detected by the lock-in. The delay line of the fundamental beam was then translated until a strong change in signal strength was detected. This corresponded to the point where both beams overlapped in time. Figure 3.21 shows the change in signal at t_0.

The dye jet was replaced by the BBO crystal. This change induced a measure of uncertainty as to the proper t_0 position of the delay line. The microscope was used

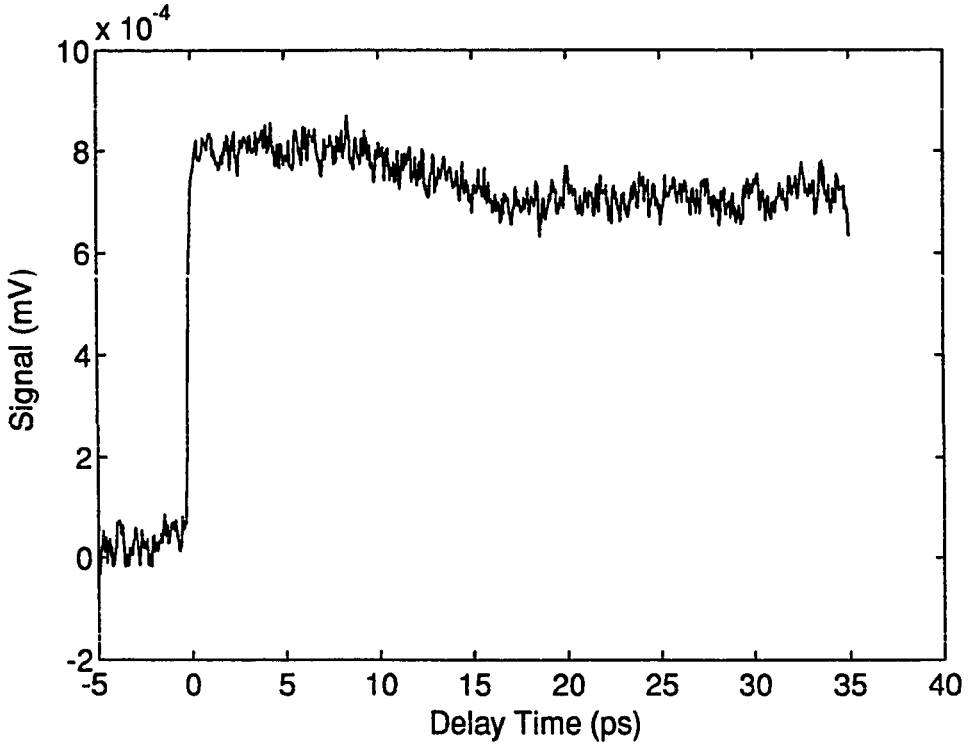

Figure 3.21: Determination of t_0 through transient bleaching in IR132 dye.

to realign the focal spots on one face of the crystal. An iterative process of angle tuning the BBO and moving the delay line around the vicinity of the measured t_0 point was used to find the correct configuration and pulse overlap to create the fourth harmonic.

3.5.2 Stage Four Measurements

The spectra of the fourth harmonic light centered at 205 nm was measured with the Monospec-18 monochromator. The entrance and exit slits were 50 μm and 25 μm wide respectively, giving an optimal resolution of 0.66 Å from Equation 2.13. The solar blind PMT was used as the detector and the preamplifier typically operated with a gain of 100. The fundamental beam was chopped at $\sim$ 2 kHz and the signal from the preamp was detected by the lock-in-amplifier.

To this point, the power generated has been too low to allow direct pulsewidth measurement. More power is required for detectable production of difference frequency mixing between the fourth harmonic and the fundamental to produce third harmonic to serve as a cross correlation measurement. Transient bleaching has also been attempted in IR140, similar to the timing technique in IR132, but no clear mea-

surement was obtained. Further methods for pulse measurement will be proposed in Chapter 5.

The power was approximated from the sensitivity of the PMT to this wavelength and the measured current from the PMT.

Case One

The spectrum for Case One had a width of 6.2 Å ± 0.66 Åas shown in Figure 3.22. This would correspond to an 100 fs pulse for a transform-limited Gaussian, the minimum pulse width possible. The maximum expected pulse width would be slightly larger, ~ 170 fs, than that of the fundamental pulse width of 159 fs due to GVD and GVM in the BBO crystal as discussed in the previous chapter.

Case Two

The spectrum for Case Two had a width of 7.3 Å ± 0.66 Å, shown in Figure 3.23. In the transform limit, this would match an 85 fs pulse. The maximum pulse width expected would be slightly larger, ~ 140 fs, due to GVD and GVM. The experimental results for both cases is shown in Table 3.5.2.

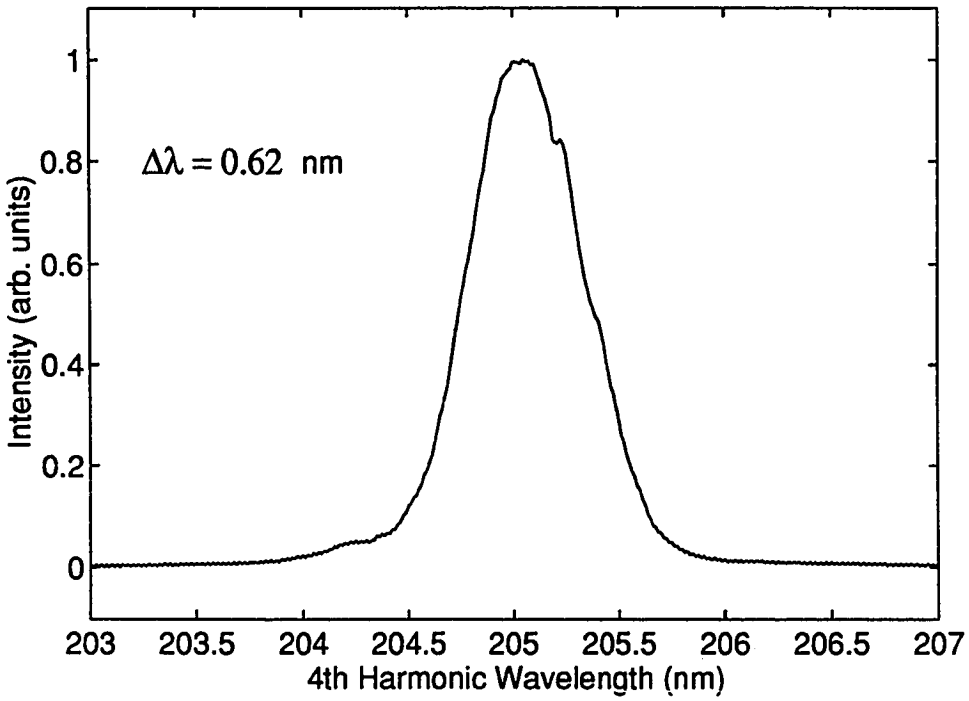

Figure 3.22: Case One: Spectrum of fourth harmonic pulses generated via SFM. The resolution of the monochromator is 0.66 Å.

	Case 1	Case 2
Power (cw)	$\approx$ 1 nW	$\approx$ 1 nW
Δt (in trans. limit)	100 fs	85 fs
Δt (approx.)	$\sim$ 170 fs	$\sim$ 140 fs
$\Delta\lambda$	6.2 Å	7.3 Å

Table 3.5: Characteristics of the fourth harmonic output. Note the pulse width Δt corresponds to the minimum possible pulse width associated with the given spectrum.

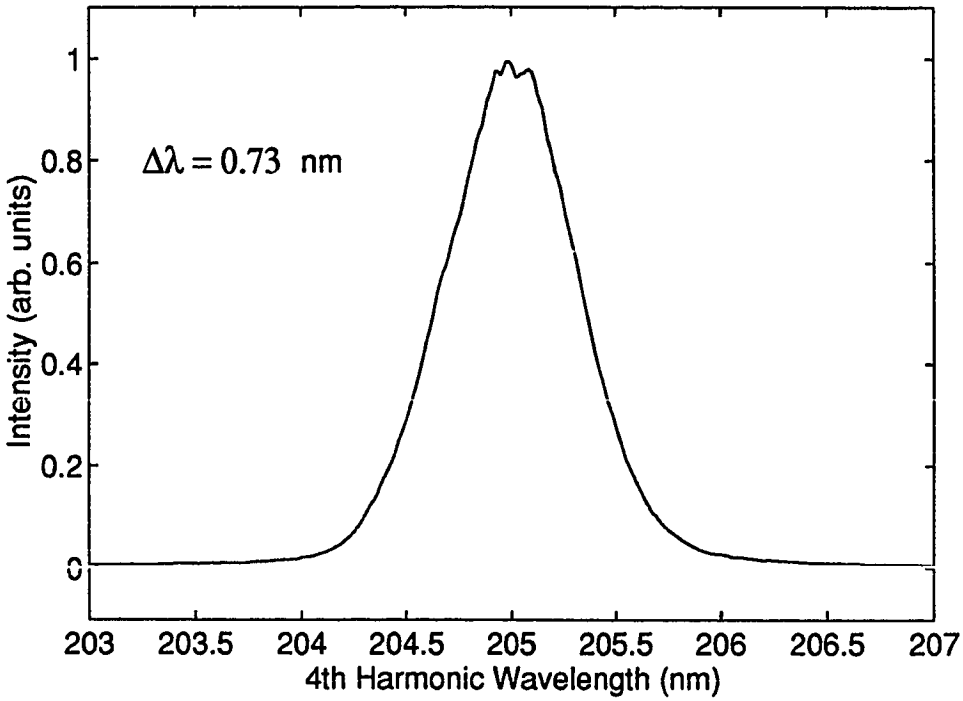

Figure 3.23: Case Two: Spectrum of fourth harmonic pulses generated via SFM. The resolution is 0.66 Å.

Chapter 4

Modeling

4.1 Modeling of Focussed SFM

4.1.1 Approach to Problem

Simple predictions for generating harmonics at short wavelengths in NLO crystals indicate that it should be impossible to create ultrashort UV laser pulses of durations less than 100 fs due to phase matching limitations on the bandwidth in available NLO crystals. This reduction in bandwidth due to the increasing dispersion at short wavelengths would lead to a 3 Å bandwidth and a corresponding 200 fs minimum pulsewidth. This would be the case if one assumed plane waves and neglected contributions to the bandwidth from cross mixing of spectral components (i.e. discounting $(\omega_1+\delta\omega)+(\omega_3-\delta\omega)=\omega_4$ contributions to $\omega_1+\omega_3=\omega_4$). The result of this calculation is shown in Figure 4.1.

Considering the measured spectra of the fourth harmonic output, this simple picture is not sufficient to explain the results of the sum frequency chain of the previous chapter. The measured spectral widths were over twice this theoretical

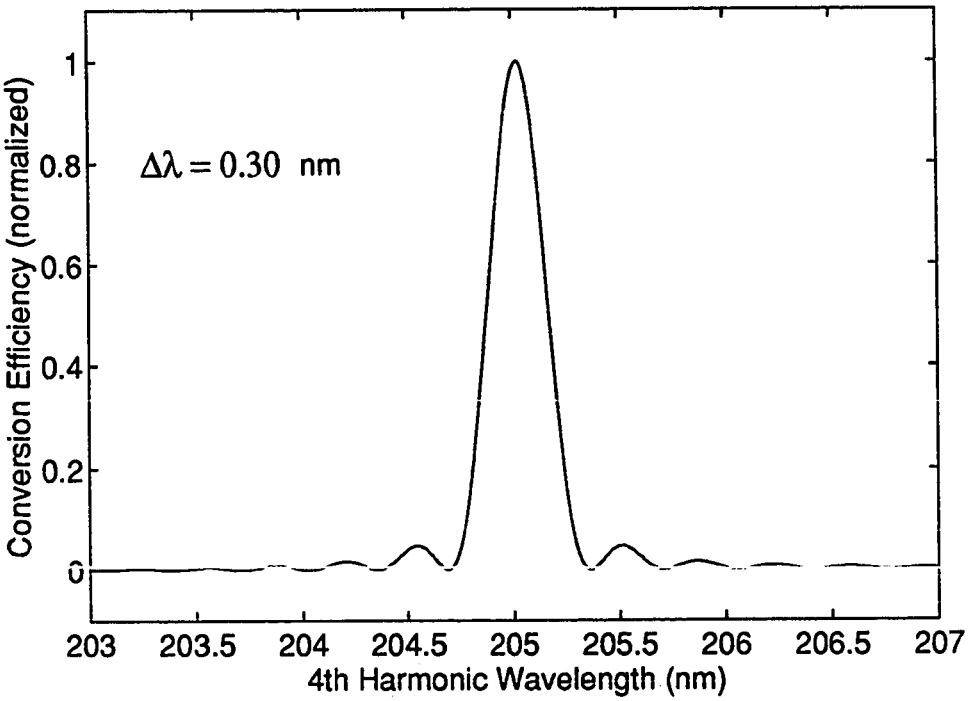

Figure 4.1: Simple bandwidth calculations yield a narrow bandwidth, limited by the spectral acceptance of the crystal.

limit. Obviously, certain important factors are neglected by this simple treatment. These factors are the extent of the bandwidths of the short pulses, the use of lenses to focus the mixing harmonics, and the positioning of the crystal with respect to the beam waists of the input beams.

In the following description of the modeling process, the two beams will be referred to as the fundamental, ω_1, and the third harmonic, ω_3, to produce the fourth harmonic, ω_4. Associated with the fundamental and the third harmonic are wavevectors $\vec{k}_1$ and $\vec{k}_3$. The angular distributions of the fundamental and third harmonic beams will be a function of the angles α and β respectively. For purpose of illustration, the following steps to model the SFM process will reflect the conditions of Case One of the preceding chapter.

4.1.2 Monochromatic SFM

In the case of two monochromatic beams, $\omega_1+\omega_3 = \omega_4$ describes the requirements due to conservation of energy that must be maintained during the harmonic generation process. This is a strict requirement. The noncollinear mixing of the two beams in a NLO crystal is described by the equation

$$|\vec{k}_4| = \sqrt{k_1^2 + k_3^2 + 2k_1k_3\cos(\phi)}, \tag{4.1}$$

where ϕ $(= \alpha + \beta)$ is the angle between the two input beams. k_4 is the magnitude of the wavevector of the generated fourth harmonic. However, $\vec{k}_4$ has a specific direction associated with its propagation. Inside the NLO crystal this direction yields a different index of refraction, $n_4(\omega_4, \theta)$ as a function of angle. n_4 taken together with the frequency ω_4 of the generated fourth harmonic yields a wavevector, $\vec{k}_{4crystal}$, where

$$|\vec{k}_{4crystal}| = \frac{n_4(\omega_4, \theta)\omega_4}{c}. \tag{4.2}$$

$\vec{k}_{4crystal}$ is collinear with $\vec{k}_4$, and the angle θ is the direction of propagation of ω_4 with respect to the optic axis of the NLO crystal. The difference between these two wave vectors is the phase mismatch, Δk, defined in Equation 2.3. Since the intensity generated at ω_4 is proportional to $sinc^2(\Delta kL/2)$, the intensity of the fourth harmonic is a function of the relative input angles and the crystal angle.

4.1.3 Finite Bandwidth SFM

The next step is to calculate the phase matching bandwidth for sum frequency generation for the spectra corresponding to short pulses. For input spectral envelopes $I_1(\omega_1)$ and $I_3(\omega_3)$, a 2-dimensional expression for the spectral mixing can be evaluated:

$$I_4(\omega_1, \omega_3) \propto I_1(\omega_1) I_3(\omega_3) sinc^2(\frac{\Delta k(\omega_1, \omega_3)L}{2}). \tag{4.3}$$

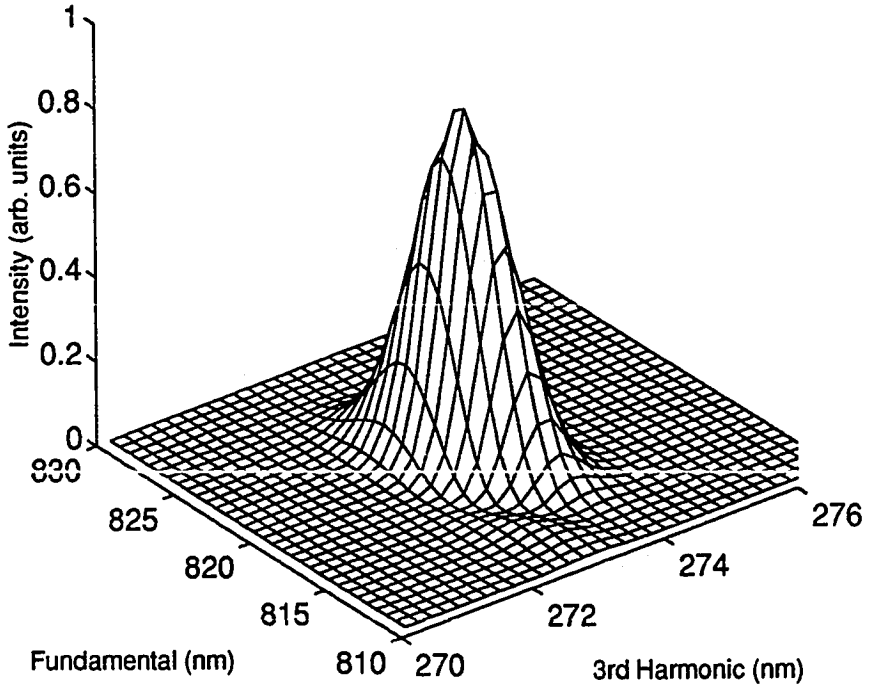

Figure 4.2: $I_4(\omega_1, \omega_3)$ **plotted in terms of wavelength.**

Shown in Figure 4.2, this 2-d surface can be reduced to the theoretical sum frequency spectrum by a simple change of variables, equivalent to a 45° rotation of the coordinate system about the z axis:

$$\omega_4 = \omega_1 + \omega_3 \quad \text{and} \quad \chi = \omega_1 - \omega_3. \tag{4.4}$$

This yields the transformation:

$$I_4(\omega_1, \omega_3) \Longrightarrow I_4(\omega_4, \chi). \tag{4.5}$$

The conversion bandwidth is then obtained by an integration over the variable χ:

$$I_4(\omega_4) = \frac{\int I(\omega_4, \chi) d\chi}{\int \int I(\omega_4, \chi) d\chi d\omega_4} \tag{4.6}$$

$I(\omega_4)$ was calculated for the conditions present in the noncollinear sum frequency mixing experiment described for Case One in Chapter 3. The results are shown in Figure 4.3. The bandwidth is 4.1 Å, still insufficient to explain the experimental measurements.

4.1.4 Finite Bandwidth SFM including Focusing Effects

The experimental configuration described in this work has finite beam diameters with lenses focusing the beams into the crystal to achieve higher intensities during the SFM

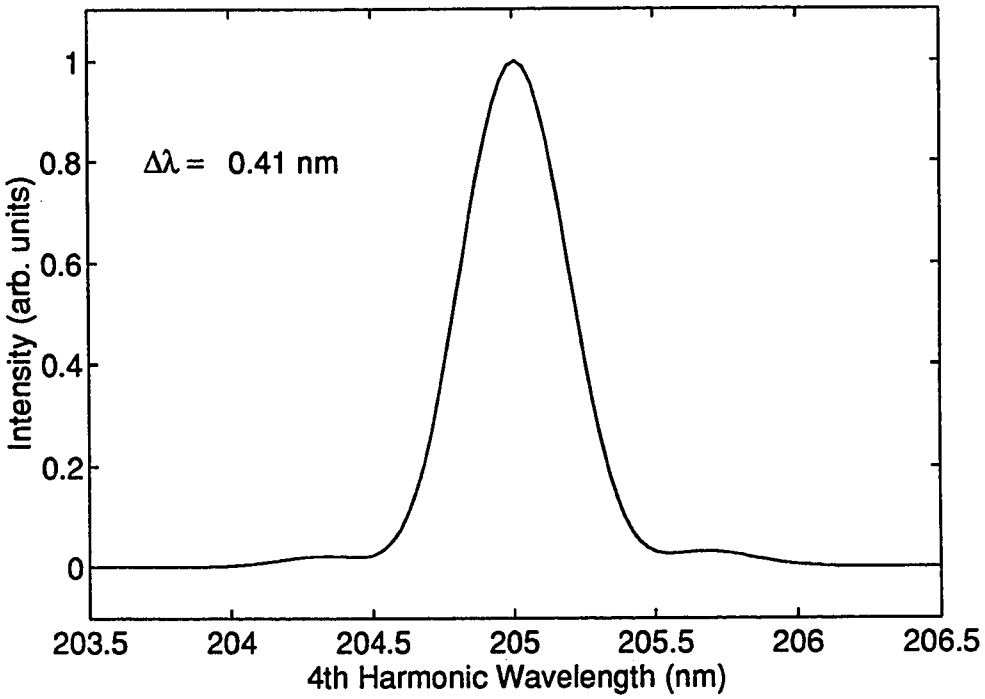

Figure 4.3: Calculated intensity distribution

process. This is shown in Figure 4.4. α denotes the angle between the ω_1 beam and the surface normal. Likewise, β is the angle between the ω_3 beam and the surface normal.

The focusing of the finite beam diameter causes an angular distribution of the input wavelengths. For each given pair of mixing spectral components there is an associated angle in the NLO crystal where efficient phase matching occurs. When focusing, different spectral components will travel along paths over a range of angles determined by the focal length of the lenses used and the diameter of the input beams.

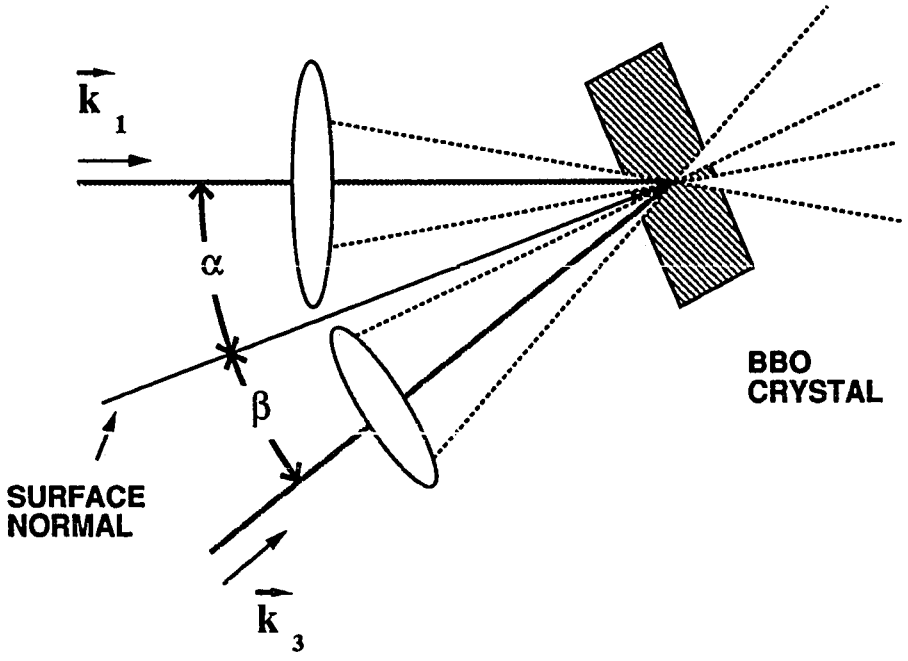

Figure 4.4: Angular distribution of focused finite beams.

Of course, this purely geometric approach will fail in the immediate vicinity of the focus and the more accurate description of Gaussian optics must be considered.

During focusing by refractive optics, short pulses behave differently than cw light due to group velocity effects [30]. However, with the small beam diameters used in this experiment, the consequences of the delay of the pulse front do not pose a significant contribution to the phase front evolution when the pulse is near the focus. The relative phase difference between the peripheral and axial sections of the pulse front would correspond to a 30 fs and a 8 fs delay for the third harmonic and fundamental beams respectively. This effect is negligible and is disregarded in the following treatment.

Focusing Parameters

Throughout the focal region, there is a continual evolution from a spherical phase front, as is the case for geometrical optics, to a phase front corresponding to a plane wave at the focal plane as depicted in Figure 4.5. The direction of propagation is perpendicular to the phase front.

Following the standard treatment of the focusing of Gaussian beams [31], the angular information contained in the phase front can be readily calculated for a

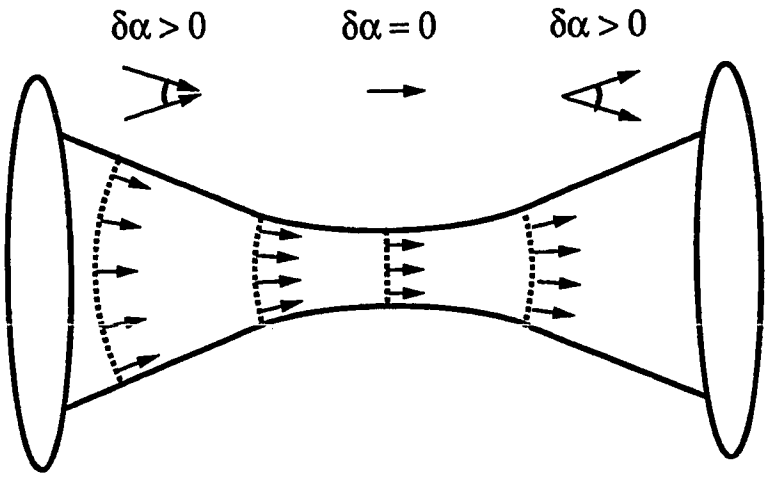

Figure 4.5: The evolution of the phase front, denoted by the dashed lines, through a confocal system. $\delta\alpha$ denotes the angular range.

diffraction limited case. The angular range, $\delta\alpha$ as shown in Figure 4.5, gives the extent of the curvature of the phase front. The angular ranges for both beams, $\delta\alpha$ for ω_1 and $\delta\beta$ for ω_3, are calculated from the radius of curvature of the phase front and the beam size:

$$\delta\alpha(z) = 2\tan^{-1}\left(\frac{w(z)}{R(z)}\right), \tag{4.7}$$

where the radius of curvature, $R(z)$, and beam radius, $w(z)$, are functions of the distance z from the focus. $\delta\beta$ would be calculated with the appropriate radius and curvature for the ω_3 focusing conditions. Figure 4.6 depicts the physical meaning of

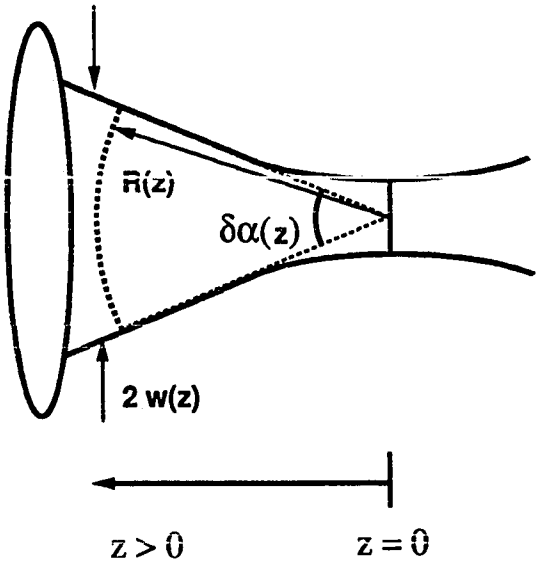

Figure 4.6: Physical definition of the radius of curvature, $R(z)$, and beam radius, $w(z)$. The dashed line represents the phase front and is shown in the geometrical optics limit. $\delta\alpha(z)$ is the angular extent of the phase front determined by $R(z)$ and $w(z)$.

the radius of curvature and beam radius. Note that the radius as shown is in the geometrical limit $z > 0$. $R(z)$ and $w(z)$ are defined in the usual manner:

$$R(z) = z[1 + \left(\frac{z_o}{z}\right)^2] \text{ and } w^2(z) = w_o^2[1 + \left(\frac{z}{z_o}\right)^2], \tag{4.8}$$

with w_o representing the beam waist radius and z_o the confocal parameter. The standard definitions of w_o and z_o are

$$w_o = \frac{2\lambda}{\pi}\frac{F}{D} \text{ and } z_o = \frac{\pi w_o^2}{\lambda}. \tag{4.9}$$

$2z_o$ is the Rayleigh range and $2w_o$ is the diameter of the beam waist. F is the focal length of the lens involved. D is the diameter of the aperture or beam. λ is the wavelength of the focused light.

Figure 4.7 shows the angular ranges, $\delta\alpha$ and $\delta\beta$, as a function of distance from the focus for ω_1 and ω_3. This corresponds to beam sizes of 2 mm diameter. ω_1 is focused with a 25 mm focal length lens and ω_3 is focused with a 50 mm focal length lens. The Rayleigh range centered on the focal plane is 320 μm for ω_1 and 440 μm for ω_3. The diameter of the beam waists in the diffraction limit would be 13 μm for ω_1 and 9 μm for ω_3.

The angular range for both beams changes drastically near the focus, dropping to zero at the focal plane. However, sum frequency mixing can occur with the nonlinear

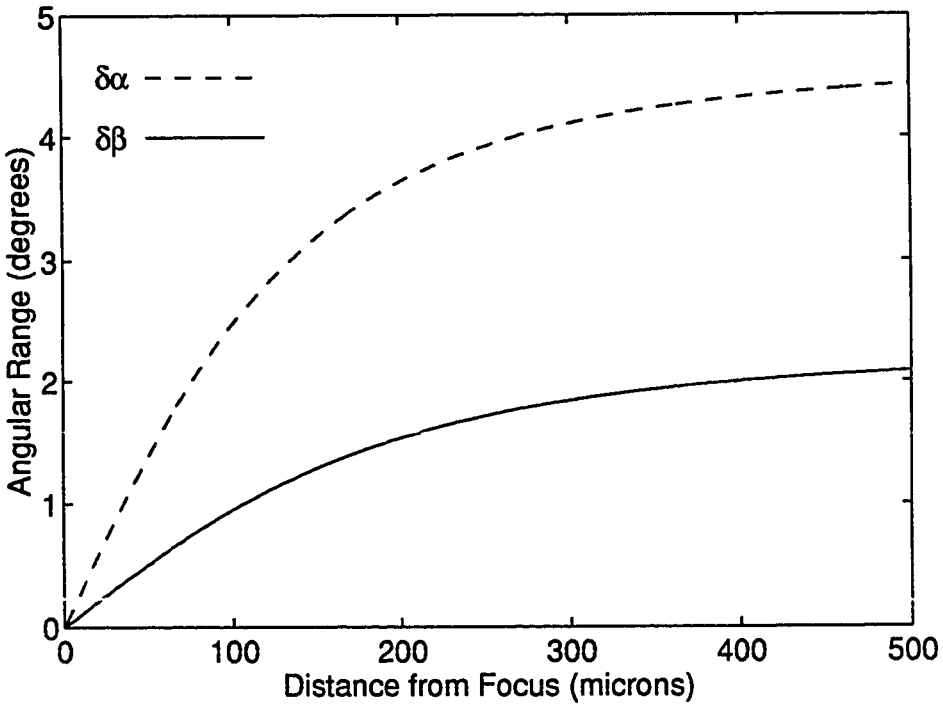

Figure 4.7: The angular ranges, $\delta\alpha(z)$ and $\delta\beta(z)$, corresponding to the focusing conditions in the 4th stage of the sum frequency chain. As the distance from the focus increases, the angular ranges approach the geometrical optics limits, 4.65° for ω_1 and 2.27° for ω_3.

crystal placed anywhere in the Rayleigh ranges of the two overlapping beams with only a slight decrease in intensity. In the physical experiment, exact alignment of the two focal planes is difficult to achieve and undesirable from the aspect of generating broad output spectra. Figure 4.8 shows two focusing conditions, one with the focal planes coincident within the BBO and one where the BBO has been shifted a short distance from the focal planes. The beam diameters have been exaggerated for purposes of illustration. The thickness of the crystal and the length of the Rayleigh ranges are to scale.

Figure 4.8(a) shows the standard method of focusing into a crystal to perform SFM. The focal planes for both ω_1 and ω_3 are coincident. As a result, the phase fronts in the mixing region are planar. $\delta\alpha(z = 0)$ and $\delta\beta(z = 0)$ are both zero. This is equivalent to the conditions used to calculate the spectum shown in Figure 4.3 where the bandwidth is 4.1 Å.

Figure 4.8(b) shows the focusing conditions for a situation where the crystal has been shifted $\sim$ 100 μm from the focal planes. This corresponds to having an angular distribution in the spectral components that are mixing within the crystal. $\delta\alpha(z = 100\ \mu m)$ is 2.46° and $\delta\beta(z = 100\ \mu m)$ is 0.96°.

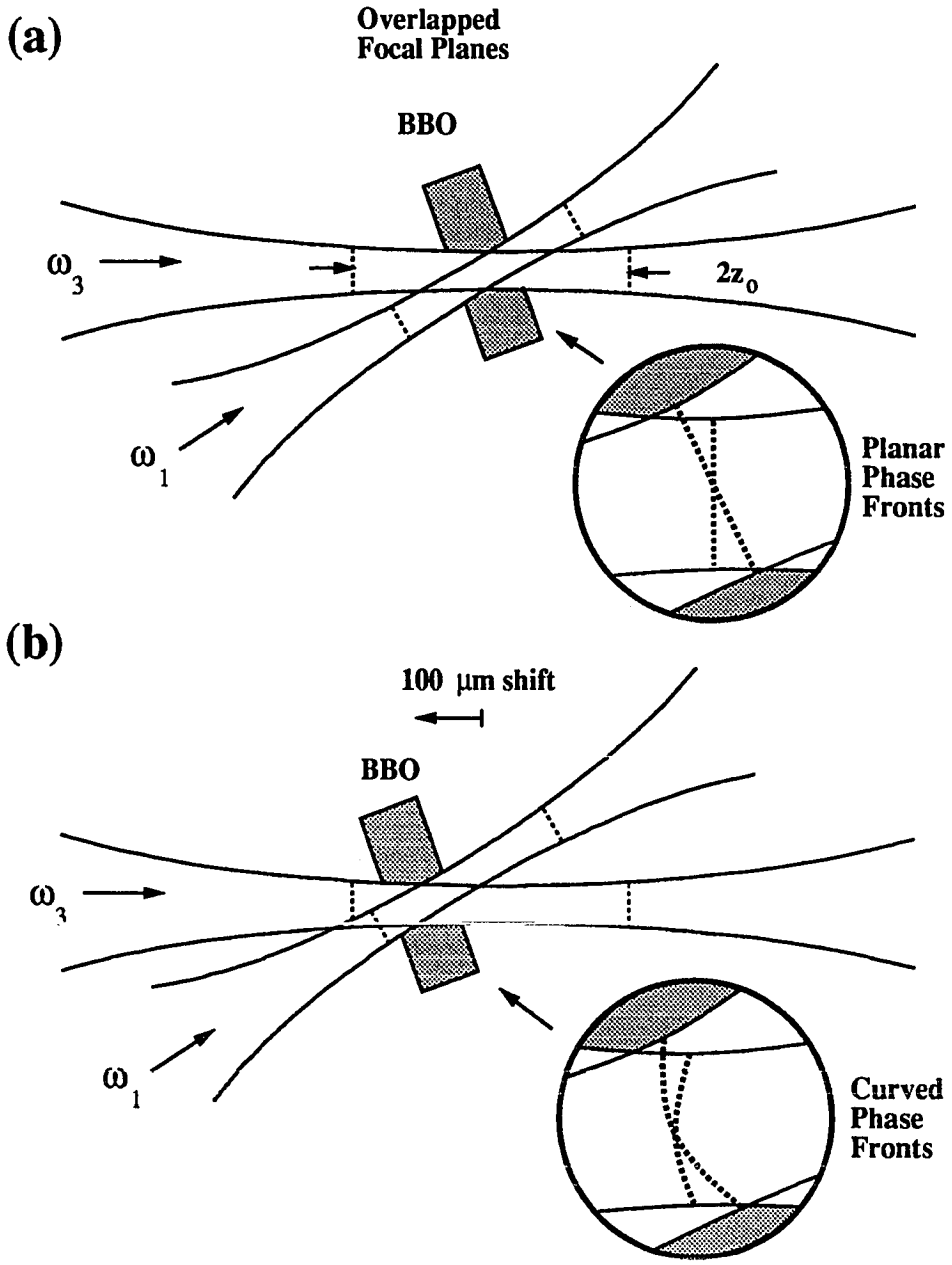

Figure 4.8: (a) shows the configuration for overlapping focal planes. The smaller dashed lines in the focusing beams indicate the Rayleigh ranges, $2z_o$. The inset displays a magnified view of the interaction region where the phase fronts are planar. (b) shows the configuration where the crystal is shifted 100 μm from the focal planes. The inset shows curved phase fronts within the crystal.

Modeling of Focusing in SFM

Once the angular ranges are calculated, $\delta\alpha$ and $\delta\beta$ are used to determine the angular intensities for ω_1 and ω_3. The angular range determines the e^{-1} width of the Gaussian distributions assumed for the angular intensity dependences, $A_1(\alpha)$ and $A_3(\beta)$. The angular ranges, $\delta\alpha(z)$ and $\delta\beta(z)$ for ω_1 and ω_3 will be considered constant over the interaction region for the sake of simplicity. Figure 4.1.4 shows $A_3(\beta)$ at a point 100 μm from the focus. $A_1(\alpha)$ would be modeled in the same way. α and β are the angles as defined in Figure 4.4.

To incorporate the effect of focusing into the bandwidth calculation, an angular mixing intensity, $F(\alpha,\beta)$, is defined as:

$$F(\alpha,\beta) = A_1(\alpha)A_3(\beta), \tag{4.10}$$

where $A_1(\alpha)$ and $A_3(\beta)$ are the angular intensity distributions of the third harmonic and fundamental beams. Figure 4.10 shows the angular mixing intensity, the product of the input intensities for every possible combination of angles α and β. The integral of the angular mixing intensity is proportional to the total input power from the fundamental and third harmonic. The logical extension of the angular mixing intensity $F(\alpha,\beta)$ is to define an angular conversion efficiency as the conversion efficiency

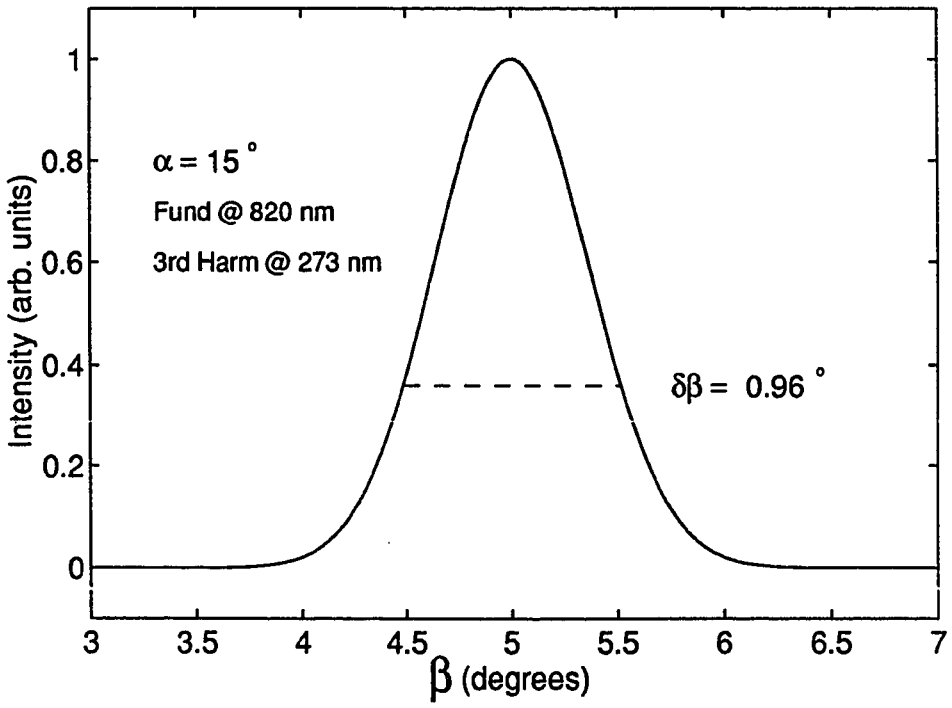

Figure 4.9: Third harmonic angular dependence of phase matching for monochromatic beams as measured from the surface normal of the BBO crystal. $\delta\beta$ corresponds to the $\frac{1}{e}$ width as calculated at $z = 100$ μm.

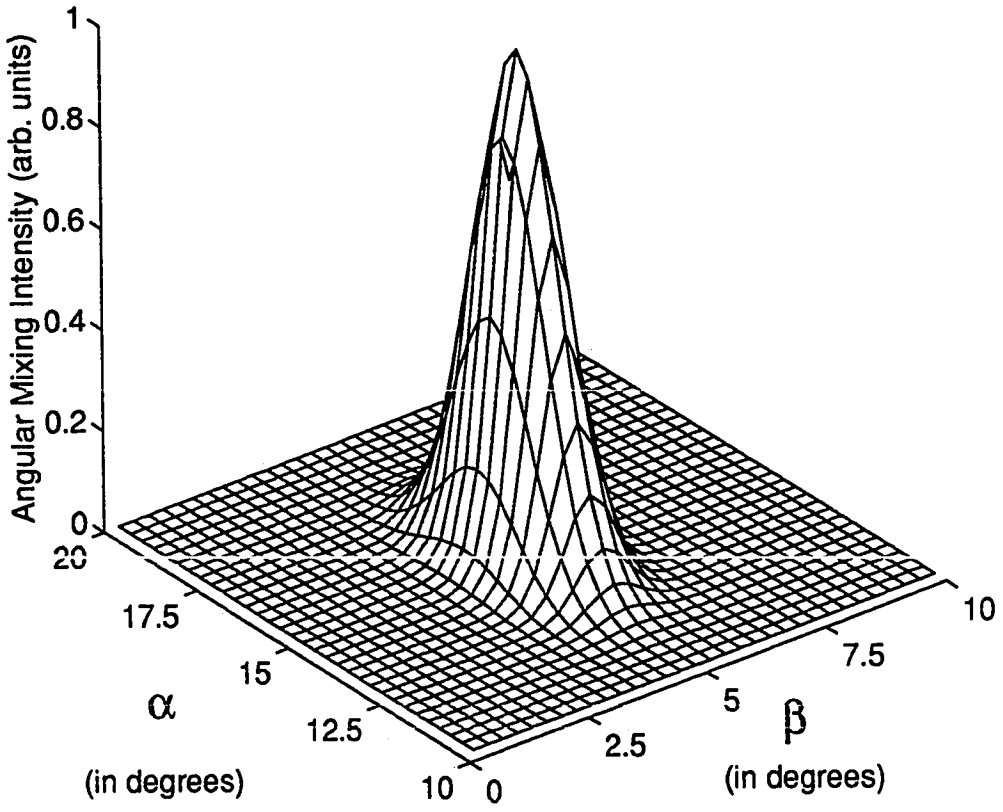

Figure 4.10: Angular mixing intensity, $F(\alpha, \beta)$, assuming a Gaussian distribution and 50 mm and 25 mm focal length lenses for the 3rd harmonic and the fundamental respectively.

determined by the phase matching limitations for a given mixing geometry. At each pair of input frequencies ω_1 and ω_3, the angular conversion efficiency, $\xi(\omega_1, \omega_3)$, is calculated:

$$\xi(\omega_1, \omega_3) = \frac{\int\int F(\alpha, \beta) sinc^2(\frac{\Delta k(\alpha, \beta, \omega_1, \omega_3) L}{2}) d\alpha d\beta}{\int\int F(\alpha, \beta) d\alpha d\beta}. \tag{4.11}$$

This angular conversion efficiency is shown in Figure 4.11. The spectral intensity of the generated sum frequency signal is then proportional to

$$I_4(\omega_1, \omega_3) \propto I_1(\omega_1) I_3(\omega_3) \xi(\omega_1, \omega_3), \tag{4.12}$$

where the functions $I_1(\omega_1)$ and $I_3(\omega_3)$ are the spectral envelopes of the input pulses, as described earlier. The function $I_4(\omega_4)$ is obtained via linear transformation and subsequent integration of $I_4(\omega_1, \omega_3)$, as described in Equations 4.5 and 4.6. In the limit of $\delta\alpha = \delta\beta = 0$, $\xi(\omega_1, \omega_3)$ would reduce to $sinc^2(\frac{\Delta k L}{2})$, making Equation 4.12 equivalent to Equation 4.3.

The result of the normalized bandwidth calculation is shown in Figure 4.12. The increase in bandwidth is close to that observed.

In the case that the beams are not focused in the diffraction limit, the beam diameters and radii of curvature would have to be adjusted. This, in turn, would change the angular ranges as a function of distance as described by Equation 4.7. An

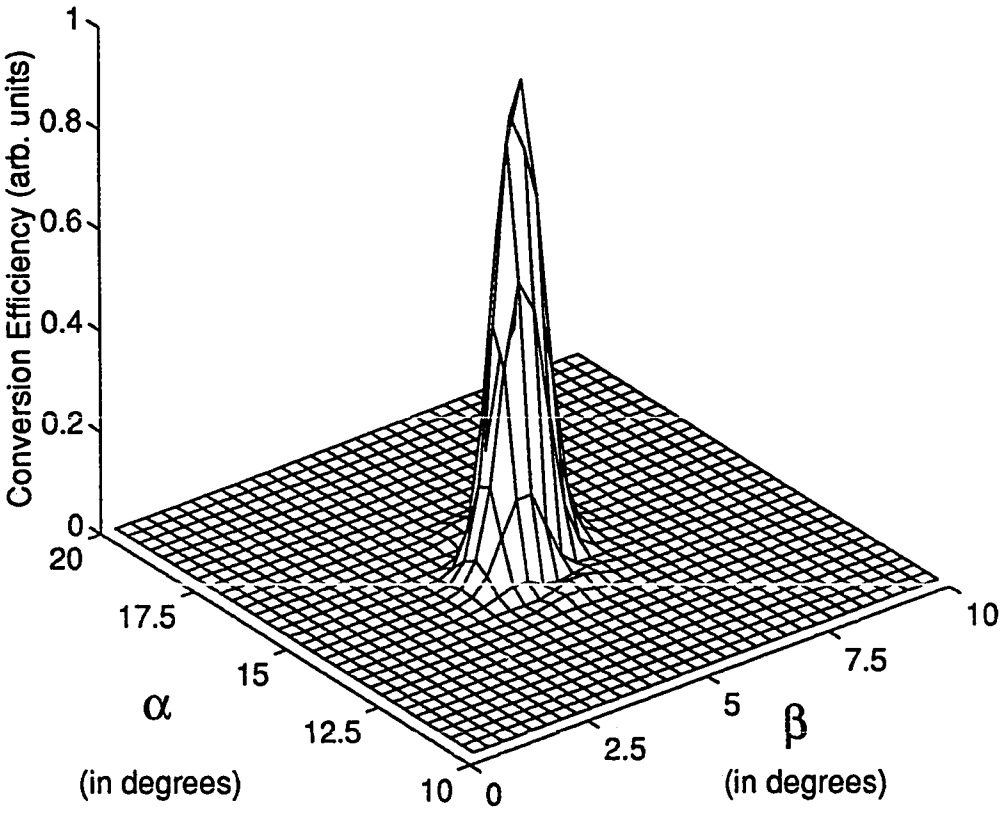

Figure 4.11: Angular conversion efficiency at the central wavelengths of 820 nm and 273.3 nm to produce 205 nm light.

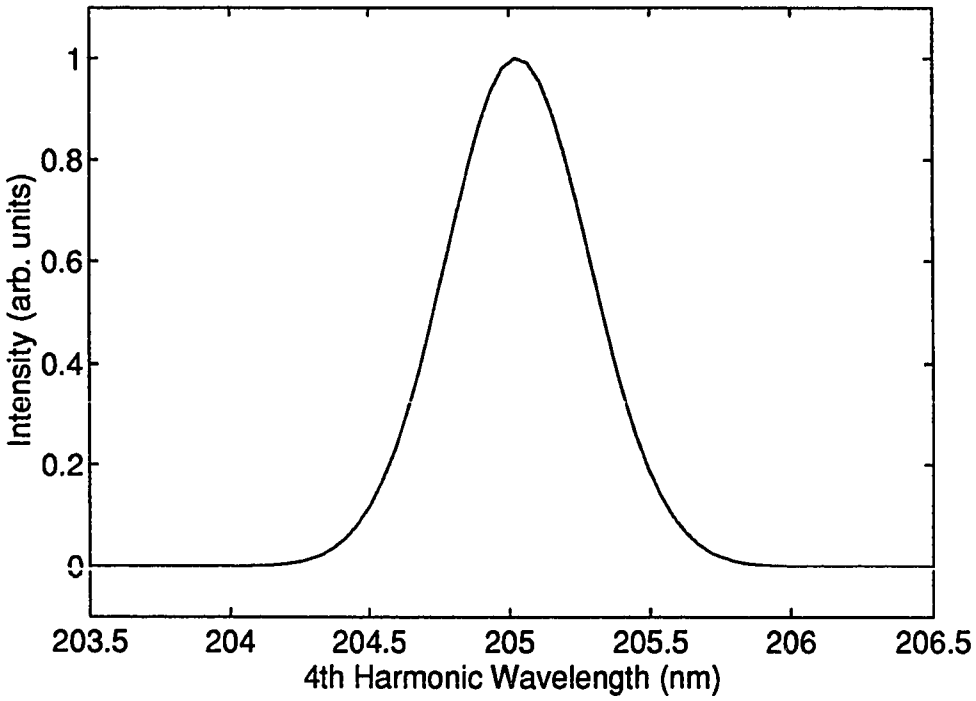

Figure 4.12: Bandwidth calculated for the 4th harmonic SFM including focusing. The bandwidth is 6 Å FWHM.

increased beam waist would result in increasing the distance between the crystal and the focal plane to achieve the same phase front curvature as the diffraction limited case.

Numerical Calculation

Numerically modeling this process required a reductionistic approach, resulting in a four step process.

1. Starting with the simplest case where two noncollinear monochromatic beams mix in a crystal, consider only the angular dependence of phase matching due to the variation of intensity across the spatial profile of one beam. The other beam maintains the same fixed angular relationship to the crystal.

2. Change the angle of the fixed beam by a small increment and reiterate the first step.

3. Once the entire range of angles for both input beams has been calculated, change the wavelength of one monochromatic beam and go back to the first step. All possible angles of both mixing beams are considered and the frequencies of only one beam are incremented.

4. When the entire spectral range of one beam has been covered, increment the frequency of the other beam and repeat the previously described steps.

Thus all possible angular and spectral contributions to the mixing process were taken into account.

4.2 Comparison with Experimental Results

Figure 4.13 shows the modeled results for the conditions measured for Case One in the previous chapter. This result is compared to the measured spectrum. Good agreement is evident over most of the range of the measured spectrum. Some deviation is observed at the short wavelength end, around 204 nm. However, the modeled spectrum displays a similar asymmetry, though to not as great an extent. The FWHM agree for experiment and calculation, with $\Delta\lambda_{meas} = 6.2$ Å and $\Delta\lambda_{theory} = 6.2$ Å. The theoretical fit corresponds to $z = 130$ μm. The angles α and β as defined in Figure 4.4 used for this simulation were 14.9° and 5.1° respectively.

Figure 4.14 displays the comparison between the measured spectra and the theoretical predictions for the generated fourth harmonic spectra for the corresponding parameters of Case Two. The fit corresponds to a distance of ~ 60 μm from the focal plane. The angles α and β used for the simulation were 15.3° and 4.7° respectively.

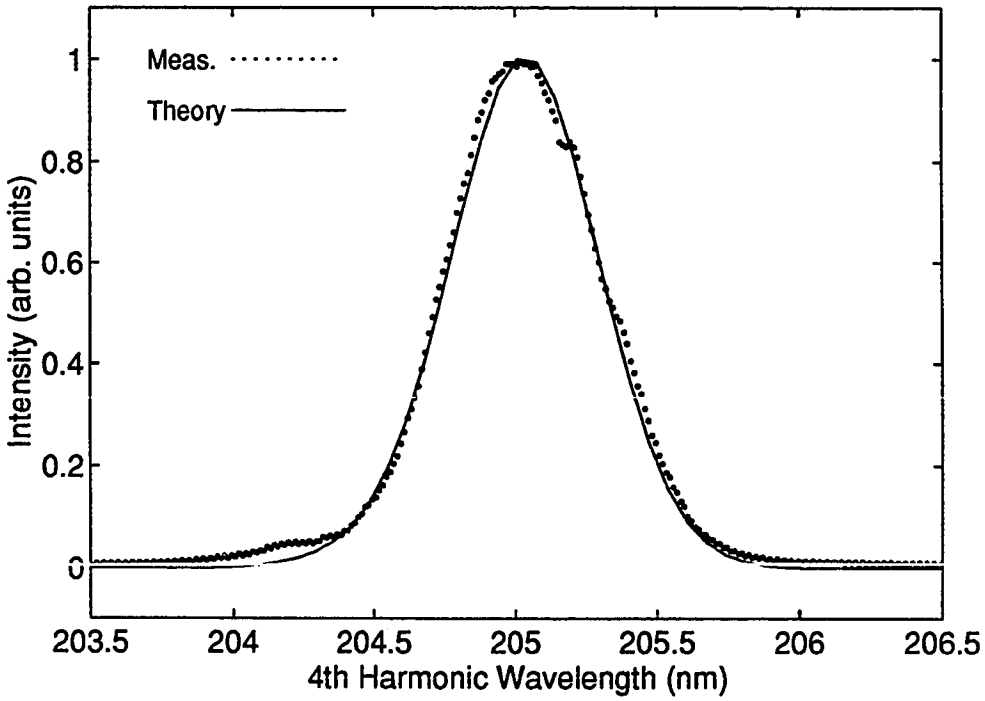

Figure 4.13: Case One: Comparison of the fourth harmonic spectrum as measured (dotted line) and as calculated (solid line).

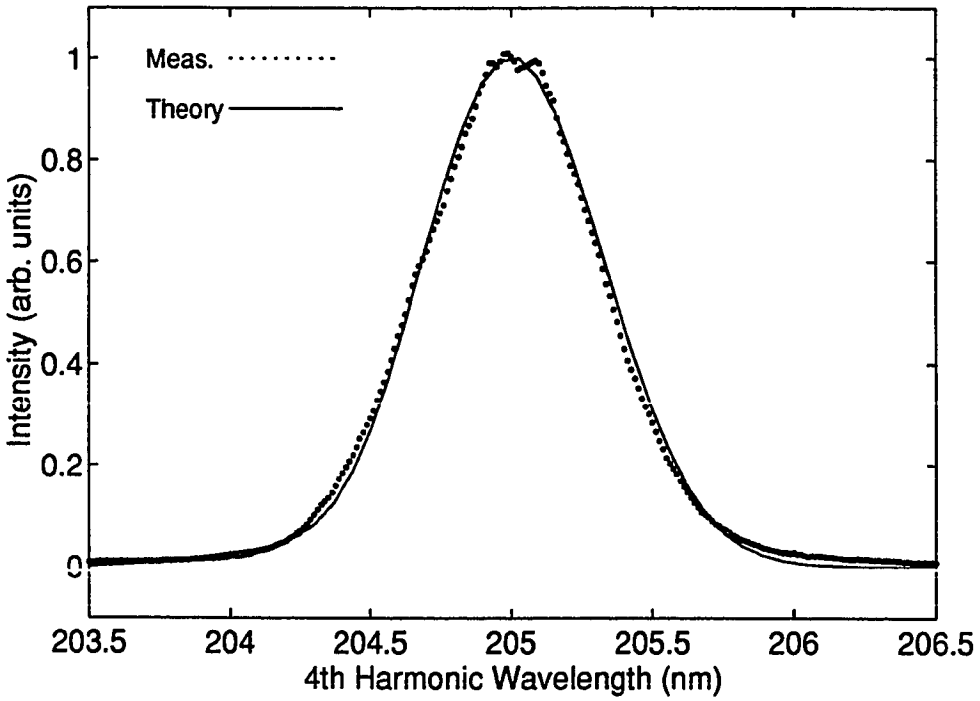

Figure 4.14: Case Two: Comparison of the fourth harmonic spectrum as measured (dotted line) and as calculated (solid line).

4.3 Predictions and Experimental Confirmation

A continual transition from the full spectral width available near the geometrical optics limit to the minimum bandwidth as limited by the crystal for input plane waves should be observable. This region should be near the focus and within the Rayleigh range to be of use in this process. The region where the focusing effects can alter the bandwidth of the generated spectra will be bounded by the plane wave limit near the focus and by the geometrical limit at larger distances z.

Changing the focusing conditions can alter the output bandwidth of the generated sum frequency light. One way to physically observe this would be to translate the lenses which focus ω_1 and ω_3. This would not serve as a good comparison as at least one of the lenses would need to be repositioned as well as the thin BBO crystal. The slightest change in the angular orientation of the BBO would result in changing the phase matching conditions and thus introduce an uncontrolled variable.

A more controlled verification is accomplished by simply aperturing the input beams as shown in Figure 3.1 before focusing. This change in beam size will in turn change the size of the beam waist and the confocal parameter. By reducing the beam diameter, the angular range for the given focusing conditions will decrease. If the

beams are well centered on the aperture and overlapping properly in the crystal, this results in a decrease in the bandwidth.

This experiment was performed with the laser operating under conditions similar to Case One. The spectrum of ω_1 had a slightly larger bandwidth at 6.9 nm and the ω_3 bandwidth was 9.8 Å. The higher power was required since the reduction in beam size corresponded to a reduction in intensity due to increased focal spot area as well as the blocking a large percentage of the incident radiation, reducing the mixing intensity, thus decreasing the ω_4 signal. The aperture was closed from 2 mm diameter to approximately 1 mm. The angular ranges change accordingly.

Figure 4.15 shows the extent of the angular range for this apertured condition as well as the angular range for the unapertured case for both ω_1 and ω_3. The Rayleigh ranges for the apertured geometry are considerably larger than the tightly focused conditions, 1500 μm for the fundamental and 2060 μm for the third harmonic. Likewise, the beam waists would be much larger at 20 μm and 14 μm diameters for the fundamental and third harmonic respectively. (The difference in beam diameter size drops the mixing intensity by a factor of 14.)

Figure 4.16 gives the ω_4 spectrum as measured with no apertures and the corresponding theoretical spectra to establish a comparison. α and β for this fit were taken

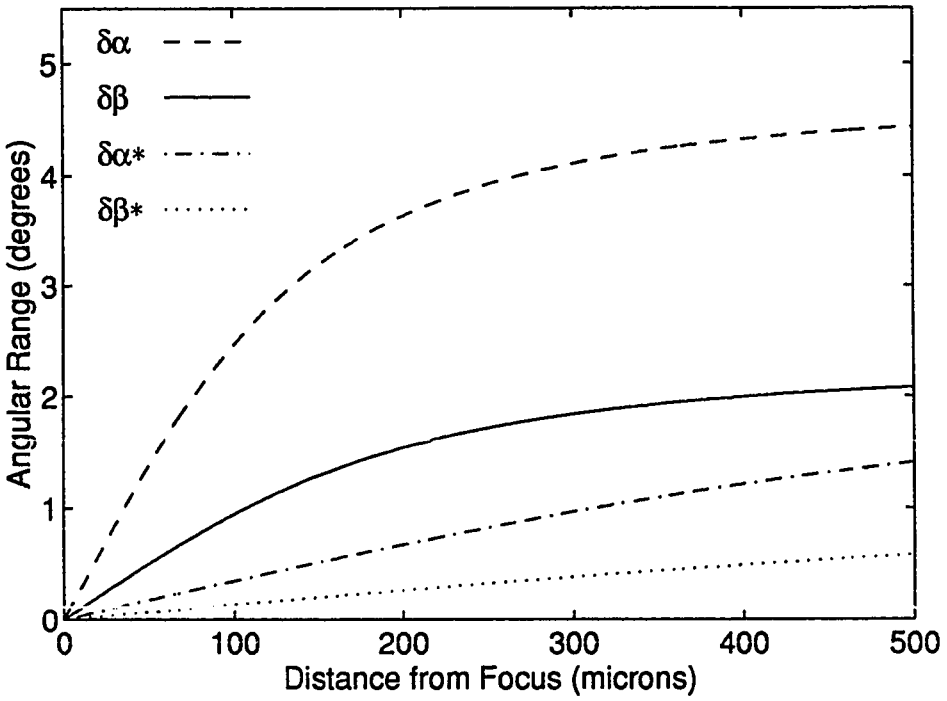

Figure 4.15: Comparison of angular ranges for apertured and nonapertured cases. $\delta\alpha$ and $\delta\beta$ are the angular ranges for the unapertured configuration. $\delta\alpha$* and $\delta\beta$* correspond to the angular ranges expected for the apertured case.

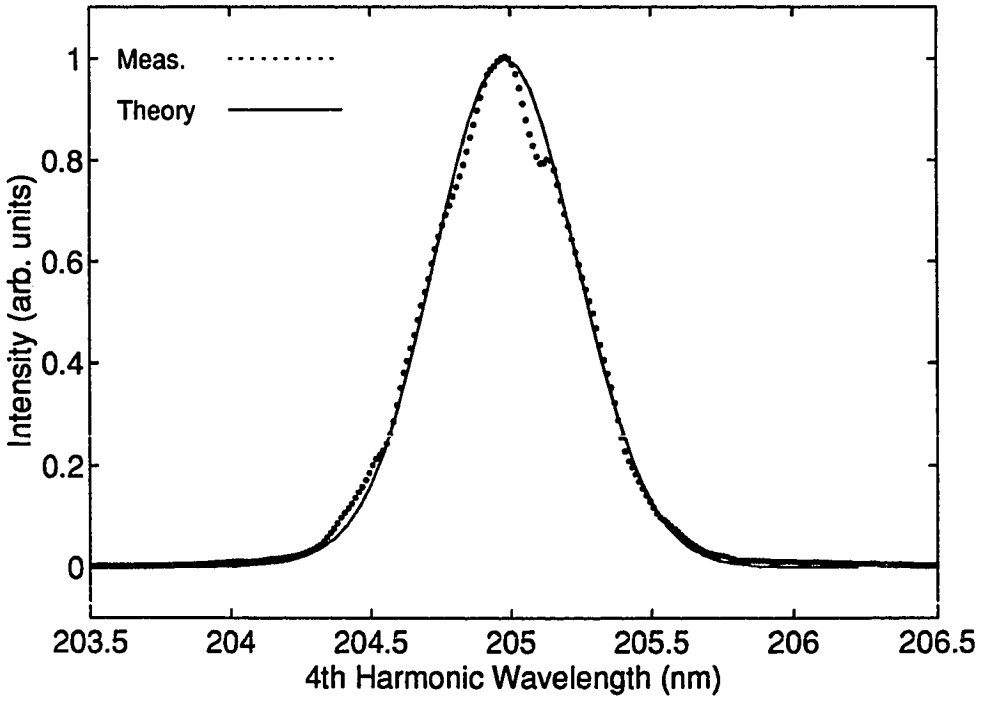

Figure 4.16: Measured and theoretical wavelength spectra for the unapertured case. The measured bandwidth is 6.4 Å under similar conditions as Case One. The bandwidth for the modeled case shows an excellent fit, FWHM 6.3 Å. The resolution of the monochromator is 0.66 Å.

to be 15.5° and 4.5° respectively. Note that α differs in this case from that shown in Figure 4.13 by only 0.6°. The values of the angular ranges $\delta\alpha$ and $\delta\beta$ match those for a distance $z = 100$ μm from the focal plane. The predicted and experimental spectra show excellent agreement. Figure 4.17 shows the result of the measurement of the fourth harmonic spectrum. The only change between Figure 4.16 and Figure 4.17 is the aperture width. The theoretical predictions yield a somewhat larger bandwidth of 4.9 Å FWHM than the measured FWHM of 4.5 Å. While the difference is below

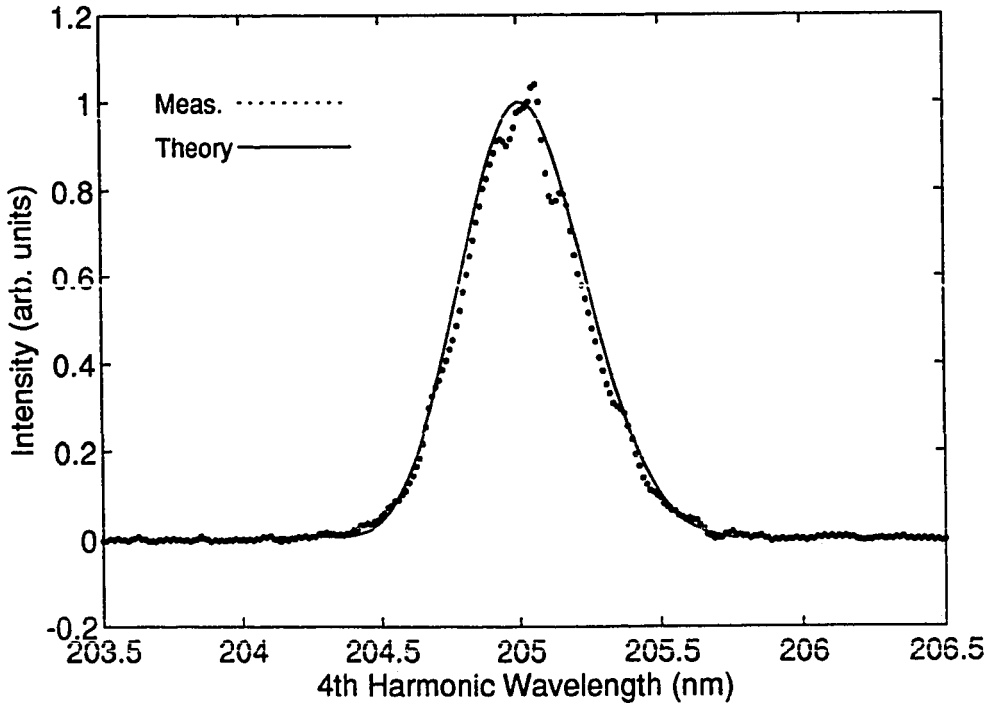

Figure 4.17: Measured and theoretical wavelength spectra with the apertures closed down to 1 mm diameter. The measured FWHM is 4.5 Å and the theoretical prediction shows a 4.9 Å bandwidth. The resolution is 0.66 Å.

the resolution limit of the monochromator, 0.66 Å, this behavior is expected as it is unlikely that the apertured beam profile would remain a precise Gaussian distribution as used in the modeling process nor would the two beams maintain the same overlap in the crystal.

In addition to providing an explanation of the broad bandwidths observed in the generation of ω_4 with tight focusing, this method also allows one to judge the distance from the focal plane.

$\Delta\lambda$ (FWHM)	Measured	Theory
2mm Aperture	6.4 Å	6.3 Å
1mm Aperture	4.5 Å	4.9 Å
Planewave Limit	4.1 Å	—

Table 4.1: Measurement and modeling results.

Chapter 5

Conclusions

5.1 Conclusion

A method for producing ultrashort light pulses in the near VUV through a successive series of sum frequency mixing stages for a Ti:Al_2O_3 laser is demonstrated. The characteristics of the sum frequency chain are shown for each harmonic frequency produced. An unexpectedly broad bandwidth—50% larger than predicted by simple calculations—is observed in the final stage, where the fourth harmonic of the Ti:Al_2O_3 laser source is generated.

A careful theoretical examination of the sum frequency mixing process points to the importance of focusing and the position of the crystal within the Rayleigh range of the mixing beams. A numerical method is developed to predict the increased bandwidth that considers the broad spectra of short pulses, the finite extent of the input beam diameters, and the placement of the crystal with respect to the focal planes of the input beams. Good agreement is found between the theory and observations for pulses on the order of 100 fs duration.

While a focusing geometry may allow sufficient bandwidth in the generated fourth harmonic for pulses on the order of 100 fs, much shorter pulses, hence broader input spectra, may not be accommodated. Dispersive mixing schemes may then become necessary to produce short pulses in the near VUV.

5.2 Improvements

One of the processes that could be improved would be the use of Type II phase matching in the third stage for the production of ω_3. Type II phase matching allows the two mixing beams, ω_1 and ω_2 in this instance, to interact in the crystal while having orthogonal optical polarizations. This would reduce the number of optics required, increasing the available power for the final stage and simplifying the experimental geometry. Initial work has been done to enact this change, but the power observed in the ω_3 beam has not been sufficient at ~ 40 μW, compared to previously measured powers of 100+ μW.

The main aspect of the SFM chain that could be changed to improve the performance would be the total power from the Ti:Al_2O_3 laser source. A factor of 5 increase in the initial power, from 200 mW to 1 W, could increase the power of the fourth harmonic by over 600%. This would allow direct pulsewidth measurement via

difference frequency mixing as well as providing sufficient output power to readily couple the various harmonics into experimental applications.

Bibliography

[1] W. Muckenheim, P. Lokai, B. Burghardt, and D. Basting, Appl. Phys. B **45**, 259 (1988).

[2] M. Sander, U. Brummund, K. Luther, and J. Troe, J. Phys. Chem. **97**, 8378 (1993).

[3] J. R. Goldman and J. A. Prybyla, Phys. Rev. Lett. **72**, 1364 (1994).

[4] L. Ziegler and B. Hudson, Opt. Comm. **32**, 119 (1980).

[5] T. Hofmann, K. Mossavi, F. Tittel, and G. Szabo, Opt. Lett. **17**, 1691 (1992).

[6] J. Krasinkski and A. Sieradzan, Opt. Comm. **26**, 389 (1978).

[7] F. Zernike and J. Midwinter, *Applied Nonlinear Optics*, John Wiley and Sons, 1973.

[8] Y. R. Shen, *The Principles of Nonlinear Optics*, John Wiley and Sons, 1984.

[9] A. Yariv, *Quantum Electronics*, John Wiley and Sons, 1989.

[10] N. Bloembergen, *Nonlinear Optics*, W. A. Benjamin, 1965.

[11] P. A. Franken and J. F. Ward, Rev. Mod. Phys. **35**, 23 (1963).

[12] R. Fork, H. Avramopoulos, and J. Valdmanis, American Scientist **78**, 216 (1990).

[13] S. Akhmanov, V. Vysloukh, and A. Chirkin, *Optics of Femtosecond Laser Pulses*, American Institute of Physics, 1992.

[14] K. Sala, G. Kenney-Wallace, and G. Hall, IEEE J. of Quant. Electron. **QE-16**, 990 (1980).

[15] J. Chilla and O. Martinez, Opt. Lett. **16**, 39 (1991).

[16] J. Goodberlet and P. Hagelstein, Opt. Lett. **18**, 1648 (1993).

[17] K. Hata, M. Watanabe, and S. Watanabe, Appl. Phys. B. **50**, 55 (1990).

[18] J. Armstrong, Appl. Phys. Lett. **10**, 16 (1967).

[19] K. D. Moller, *Optics*, University Science Books, 1988.

[20] D. Eimerl, L. Davis, L. Velsko, E. Graham, and A. Zalkin, J. Appl. Phys. **62**, 1968 (1987).

[21] R. A. Cheville, M. T. Reiten, and N. J. Halas, Opt. Lett. **17**, 1343 (1992).

[22] G. Szabo and Z. Bor, Appl. Phys. B **50**, 51 (1990).

[23] A. Nebel and R. Beigang, Opt. Comm. **94**, 369 (1992).

[24] J. Ringling, O. Kittelmann, and F. Noack, Opt. Lett. **17**, 1794 (1992).

[25] J. Ringling, O. Kittelmann, F. Noak, G. Korn, and J. Squier, Opt. Lett. **18**, 2035 (1993).

[26] N. Sarukura, Y. Ishida, H. Nakano, and Y. Yamamoto, Appl. Phys. Lett. **56**, 814 (1990).

[27] N. Sarukura, Y. Ishida, and H. Nakano, Opt. Lett. **16**, 153 (1991).

[28] D. Negus, L. Spinelli, N. Goldblatt, and G. Feugnet, unpublished (1991).

[29] M. Hobden, J. of Appl. Phys. **38**, 4365 (1967).

[30] Z. Bor, J. Mod. Opt. **35**, 1907 (1988).

[31] J. Verdeyen, *Laser Electronics*, Prentice-Hall, 1989.